

What Determines the Maximum Mass of AGN-assisted Black Hole Mergers?

LINGQIN XUE,¹ HIROMICHI TAGAWA,² ZOLTÁN HAIMAN,^{3,4,5} AND IMRE BARTOS¹¹*Department of Physics, University of Florida, PO Box 118440, Gainesville, FL 32611-8440, USA*²*Shanghai Astronomical Observatory, Shanghai, 200030, People's Republic of China*³*Institute of Science and Technology Austria, Am Campus 1, Klosterneuburg 3400 Austria*⁴*Department of Astronomy, Columbia University, MC 5246, 538 West 120th Street, New York, NY 10027, USA*⁵*Department of Physics, Columbia University, MC 5255, 538 West 120th Street, New York, NY 10027, USA*

ABSTRACT

The origin of merging binary black holes detected through gravitational waves remains a fundamental question in astrophysics. While stellar evolution imposes an upper mass limit of $\sim 50M_{\odot}$ for black holes, some observed mergers—most notably GW190521—involve significantly more massive components, suggesting alternative formation channels. Here we investigate how heavy black holes merging within Active Galactic Nucleus (AGN) disks can become. Using a comprehensive semi-analytic model incorporating 27 binary and environmental parameters, we explore the role of AGN disk conditions in shaping the upper end of the black hole mass spectrum. We find that AGN disk lifetime is the dominant factor, with high-mass mergers ($\gtrsim 200M_{\odot}$) only possible if disks persist for $\gtrsim 40$ Myr. The joint electromagnetic observation of an AGN-assisted merger could therefore lead to a direct measurement of the age of an AGN disk.

1. INTRODUCTION

Binary black hole mergers are now regularly being observed through gravitational wave emission. The LIGO (Aasi et al. 2015), Virgo (Acernese et al. 2015) and KAGRA (Akutsu et al. 2019) collaborations have reported around 90 previous discoveries, while their 4th observing run, O4, is currently ongoing.

The origin of the observed black hole mergers, and the astrophysical processes that lead to the mergers, are some of the main questions of interest. These questions are not settled at present, and multiple possible astrophysical scenarios are being investigated. These include formation from isolated stellar binaries (e.g., Postnov & Yungelson 2014; van den Heuvel et al. 2017; Mandel & de Mink 2016), dynamical formation in dense clusters (e.g., Benacquista & Downing 2013; Rodriguez et al. 2016; Kocsis 2022), or gas capture in the disks of active galactic nuclei (AGNs; e.g., Bartos et al. 2017; McKernan et al. 2018; Yang et al. 2019; Tagawa et al. 2020; Dutta Roy et al. 2025).

Differentiating between these formation mechanisms for either a single detection or the overall set of detections is made difficult by both the currently large model uncertainties and the expected substantial overlap between the binary properties these mechanisms are expected to produce. A

promising direction to avoid this overlap is to specifically target outliers, or in general parts of the parameter space not expected to be covered by all models.

The high end of the observed black hole mass distribution is a particularly promising part of the parameter space. Generally, heavier black holes are expected to be rarer, making processes that preferentially select heavier black holes for mergers stand out. Even more importantly, black hole formation from stellar evolution is expected to reach only up to a mass of around $50M_{\odot}$ (Fryer et al. 2001). Massive stars above a critical mass are expected to experience pair instability in their center, resulting in their early explosion before they could form a sufficiently massive core. These stars are expected to leave no compact remnant behind, effectively putting an upper limit on how massive black holes can be formed from stars.

Black holes have nonetheless been observed with over $50M_{\odot}$ mass. In particular, merger GW190521 was recorded to have been a binary of two black holes with masses estimated to be $95.3^{+28.7}_{-18.9}M_{\odot}$ and $69.2^{+17.0}_{-10.6}M_{\odot}$ (Abbott et al. 2020, 2021). Such high masses are difficult to explain with stellar evolution (although see Belczynski 2020). In addition, GW190521 featured other outlying properties, including its apparent high precessing spin, and possibly highly eccentric orbit prior to merger (Gayathri et al. 2022; Romero-Shaw et al. 2020; Gamba et al. 2023), pointing towards a dynamical or AGN origin (Samsing et al. 2022).

A promising mechanism to explain the creation of black hole masses beyond stellar evolution limits is the consecutive merger of black holes, or so-called *hierarchical mergers* (Gerosa & Berti 2017; Fishbach et al. 2017; Yang et al. 2019; Tagawa et al. 2020b, 2021; Mahapatra et al. 2021, 2024, 2025). The remnant of the merger of two black holes can naturally exceed the maximum mass allowed by stellar evolution, therefore, if such remnants can participate in further mergers, possibly much higher black hole masses can be reached.

How high the masses can get depends on the physical processes and environmental conditions that produce the hierarchical mergers, and possibly accretion.

In this paper we explore this connection between maximum mass and environment. The goal of this investigation is to understand how the observation of the heaviest black holes can be converted to understanding of the environment of the black holes, or astrophysical processes more generally.

We will in particular focus on black hole mergers in AGN disks. AGNs are promising black hole assembly lines that are expected to promote hierarchical mergers (Yang et al. 2019), while also may grow black hole masses through accretion (Yang et al. 2020).

AGN-assisted mergers represent possibly the most complex binary evolution process that features not only the properties of populations of compact objects and stars but also accretion and interaction with the AGN disk. This complexity means that there are a large number of binary and environmental parameters, many of which are not well understood. We will include 27 such parameters in our model, which are described in Table 1. Due to the difficulty of exploring a 27-dimensional parameter space, our strategy is to consider a fiducial value for each parameter, and explore the change of the maximum mass compared to the fiducial value by changing only a single parameter at a time. This gives an informative picture of the dependence of the maximum mass on each of the 27 parameters.

As there is no hard cutoff for black hole masses but rather a continuous, if steep, distribution, we will define maximum mass for the purposes of our analysis as the average mass of the heaviest 1% of the black holes that undergo mergers in our simulations for each set of parameters. This mass is informative of what is expected to be observable as the highest mass through gravitational waves from the AGN channel, and therefore we consider it a meaningful basis for observational model testing.

The paper is organized as follows. Section 2 presents our AGN model and binary gas capture, evolution and merger simulation framework. We present our results in Section 3. We discuss some of the limitations of our model and future work in 4, and conclude in Section 5.

2. METHOD

Our AGN model largely builds on the framework established by Tagawa et al. (2020b). Our main modification compared to this model aims to enable faster simulations to be able to cover a larger part of the parameter space. Instead of employing N-body simulations, we adopt a statistical approach to efficiently calculate background properties, significantly reducing computational costs. Especially, this approach enables us to simulate systems with high mass SMBHs and large populations of stellar-mass BHs. Comparable studies using statistical methods have been conducted, focusing on dynamical interactions (Gondán et al. 2018) and gas interactions (McKernan et al. 2012; Vaccaro et al. 2024; Gayathri et al. 2021; Yang et al. 2019) independently. Additionally, Fokker-Planck numerical methods have been used to investigate extreme mass ratio inspirals near SMBHs (Pan & Yang 2021). Many studies also explore spin evolution due to these mechanisms (Gondán et al. 2018; Vaccaro et al. 2024; Tagawa et al. 2020a; Gayathri et al. 2021). In the present paper, we consider both the gas hardening process and star interactions, while spin evolution will be explored in a future paper.

Our simulations focus on a system consisting of multiple stellar-mass black holes (BHs) and binary BHs near a central supermassive black hole (SMBH) of mass M_{SMBH} . The system also includes a gaseous AGN disk, a background stellar distribution, and an evolving population of BHs. A flowchart summarizing the simulation framework is presented in Fig. 1, and Table 1 summarizes all free parameters and the range of values explored in our simulations.

The simulations are constrained within radial distances between r_{in} and r_{out} from the central SMBH. This radial range is divided into $N_{\text{cell}} = 120$ cells with log-uniform distribution. The inner radius, r_{in} , is set to be the inner boundary of the AGN disk, $r_{\text{disk,in}}$, while the outer radius, r_{out} , is chosen to be the minimum value of 5pc and the outer boundary of AGN disk $r_{\text{disk,out}}$ to optimize computational efficiency. We provide a convergence test in Sec 4.1.

The BH and stellar populations are described in Section 2.1, which provides their spatial and mass distribution. The Keplerian speed is slightly modified by the presence of the spatially extended stellar populations (Eq. 6).

The properties of the AGN disk are calculated using the model described in Section 2.2. The inner ($r_{\text{disk,in}}$) and outer ($r_{\text{disk,out}}$) boundaries of the AGN disk are treated as free parameters to estimate their effect, though it could be set by the innermost stable circular orbit (ISCO) of SMBH. Details are discussed in section 2.2 and 2.4.3. The simulation begins by determining the accretion rate at the outer boundary of the AGN disk, \dot{M}_{out} , and uses this to compute the disk's properties from the outer radius inward. It is assumed that stars and BHs are formed in the outer region of the AGN disk, which

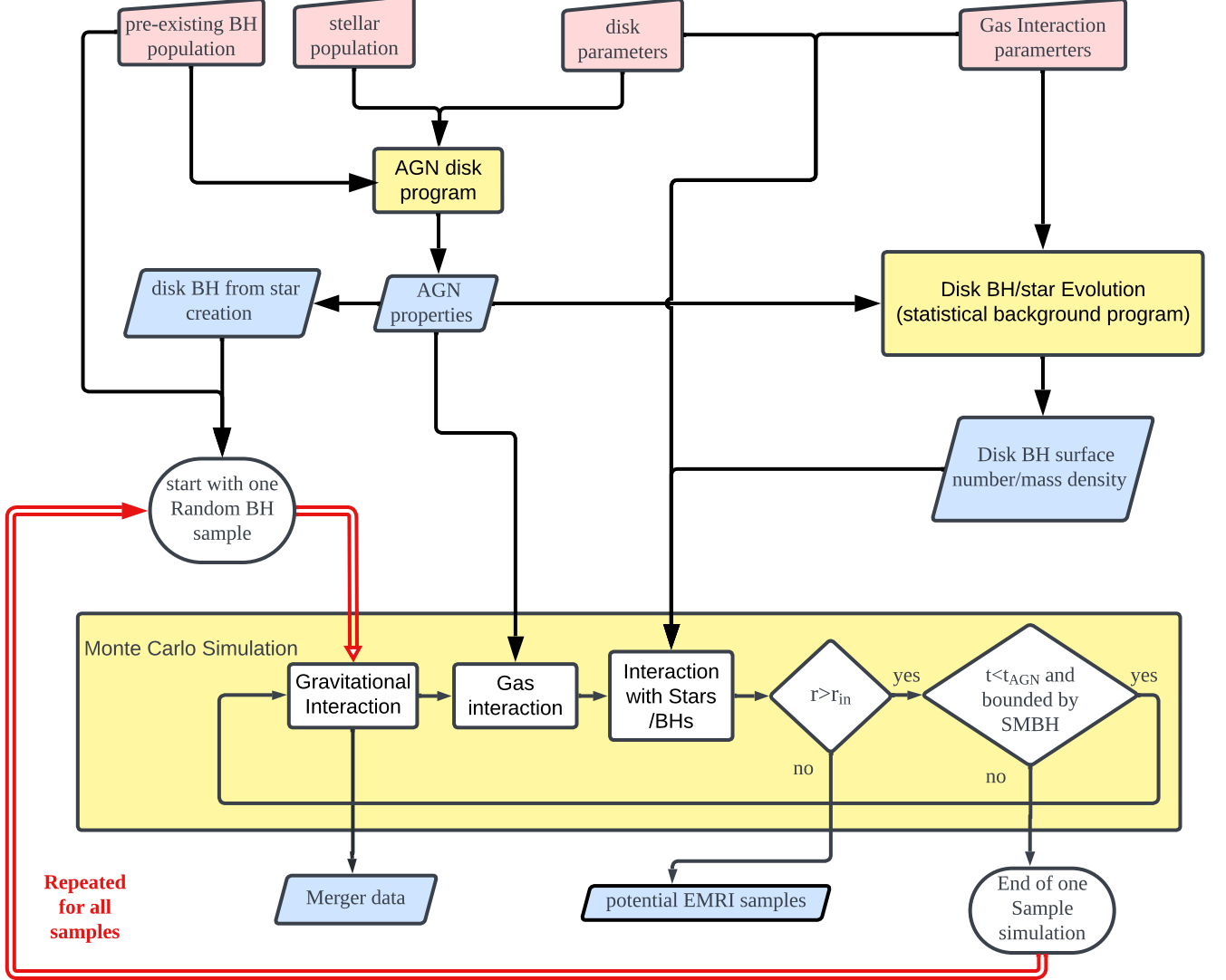


Figure 1. Schematic flow chart of the simulation framework. Pink blocks represent configurable models and parameters, including AGN disk properties, initial BH/stellar populations, and gas interaction models. Yellow blocks correspond to different computational processes, such as AGN disk property calculations, statistical background estimations, and Monte Carlo simulations for BH evolution. Blue blocks indicate simulation outputs, such as merger rates, mass distributions, and population evolution trends. The Monte Carlo simulations are repeated (red double arrows) to track BH status throughout the AGN lifetime, with iterations terminated when either 10,000 mergers are recorded or 10 AGNs are fully simulated.

helps to stabilize the disk. Star formation ceases when the accretion heat at the outer boundary is sufficient to prevent gravitational collapse. This typically occurs in systems with either a low SMBH mass or a low accretion rate at the outer boundary. Given the non-zero star formation rate, disk properties are calculated on a denser radial grid, as suggested in Section 2.2, and then translated to the standard values at grid boundaries and center of $N_{\text{cell}} = 120$.

The distribution of BHs within the AGN disk is then estimated as outlined in Section 2.6. We apply a mass step on a log-uniform scale between the minimum BH mass $M_{\text{BH,min,ini}}$

and 3 times the maximum single BH mass, $3M_{\text{BH,max,ini}}$. The joint surface number density and mass density function $\Sigma(r, M)$ evolves over time, where the total surface number density of disk BHs is given by $\Sigma_{\text{DBH}} = \int dM \Sigma(r, M)$. The background calculations' time step is discussed in Section 2.6. The time-evolving disk BH number density $\Sigma_{\text{DBH}}(r, t)$ and mass density $M_{\text{tot,DBH}}(r, t)$ are then established at the radial grid boundaries and subsequently converted to values at the cell centers for individual BH sample simulations.

With the background fully established, we begin by considering single or binary BHs, characterized by BH mass

M_{BH} , radial position r from the SMBH, velocity components $v_{x,y,z}$ relative to the disk velocity, and, for binaries, the mass ratio q and separation s . We examine the evolution of these quantities as the BHs interact gravitationally (Section 2.3), with the surrounding gas (Section 2.4) and with the surrounding stellar objects as an evolving background (Section 2.5).

Figure 2 illustrates all interaction types considered in the program. In the gravitational interaction, we discuss binary hardening due to gravitational wave emission (Section 2.3.1) and, eventually, the merger into a new single BH (Section 2.3.2). The interaction between the BH and the surrounding gas affects mass, position, and velocity through gas accretion (Section 2.4.1), gas dynamical friction (Section 2.4.2), and Type I/II migration (Section 2.4.3). Gas dynamical friction may also assist in binary formation (Section 2.5.4) and binary hardening process (Section 2.4.4). The interaction between the BH or BH binary and the evolving background includes both weak encounters (weak scattering, Section 2.5.1) and strong encounters, such as binary-single interactions (Section 2.5.2) and binary formation through three-body interactions (Section 2.5.3). These effects renew the BH sample's properties iteratively with time step given in Section 2.7 until the AGN disk dissipates.

We record all merger events that occur during the simulation, aiming for at least 10,000 mergers. However, since the merger rate varies significantly, strictly requiring 10,000 mergers may lead to excessive computational time. To balance efficiency and accuracy, we maintain a minimum of 10 AGNs if the merger rate is low, where the initial number of BHs $N_{\text{BH,ini}}$ is set by default according to Eq. 9. In the individual sample simulation, the radial distance r , Keplerian speed v_{kep} and the disk properties (e.g. gas density ρ) are represented by the cell center values to reduce computational cost.

Our program is written in C++ to optimize computational performance. The AGN disk module takes approximately 7 seconds per AGN and shows minimal variation across parameter choices, as the runtime is primarily dominated by data input/output operations. The statistical background calculation for the fiducial models (both Gaussian and isotropic) requires roughly 600 seconds (CPU time) and scales approximately linearly with the AGN lifetime and the number of time intervals specified in Eq. 113. This computational cost also decreases with increasing SMBH mass.

The runtime of the Monte Carlo simulation depends on the chosen model and parameter settings. For instance, the fiducial Gaussian model with $t_{\text{AGN}} = 10$ Myr takes 7,825 seconds (CPU time) to simulate 2 AGNs and produce 10,000 merger events. In comparison, the fiducial isotropic model with the same AGN lifetime takes 5,204 seconds (CPU time) to simulate 6.5 AGNs and yield over 10,000 merger events. The runtime does not increase linearly with AGN lifetime but in-

stead grows more slowly for longer AGN lifetime. For instance, with $t = 100$ Myr, the Gaussian model requires approximately 129,000 seconds (CPU time) to simulate a single AGN, while the isotropic model takes about 50,000 seconds. Importantly, the Monte Carlo simulations are straightforward to parallelize using the OpenMP package, enabling substantial speed-up when running on multiple CPU cores or computing nodes.

2.1. Pre-existing stellar and BH populations

In the fiducial model, the pre-existing single BH mass is drawn from the initial BH mass function, which we define as (Chabrier 2003; Salpeter 1955):

$$\frac{dN}{dM_{\text{BH}}} = \mathcal{F}_{\text{pre}}(M_{\text{BH}}) = \frac{(1 - \beta_{\text{IMF}})M_{\text{BH}}^{-\beta_{\text{IMF}}}}{M_{\text{BH,ini,max}}^{1-\beta_{\text{IMF}}} - M_{\text{BH,ini,min}}^{1-\beta_{\text{IMF}}}}, \quad (1)$$

within the range of maximum and minimum BH masses, $M_{\text{BH,ini,max}}$ and $M_{\text{BH,ini,min}}$ respectively.

We use the stellar distribution as a background parameter that remains constant at the same radial distance over time. In our fiducial model, we assume an average stellar mass $\bar{m}_* = 1M_{\odot}$ as the main sequence stellar mass, and adopt the stellar number density from O'Leary et al. (2009):

$$n_* = 1.38 \times 10^5 \text{ pc} \left(\frac{10^6 M_{\odot}}{M_{\text{SMBH}}} \right)^{1/2} \left(\frac{r}{r_i} \right)^{-1.4}, \quad (2)$$

where r_i is assumed to be the nuclear star cluster (NSC) size, determined by SMBH mass M_{SMBH} and velocity dispersion σ_* :

$$r_i = \frac{GM_{\text{SMBH}}}{\sigma_*^2}, \quad (3)$$

To avoid the singularity in our simulation and match up with the simulation result in O'Leary et al. (2009), we assume that the stellar density outside the NSC ($r > r_i$) is

$$n_* = 1.38 \times 10^5 \text{ pc} \left(\frac{10^6 M_{\odot}}{M_{\text{SMBH}}} \right)^{1/2} \exp\left(-\frac{r}{r_i}\right). \quad (4)$$

Although many recent studies have reported variations in the index of the $M - \sigma$ relation of NSC (McConnell et al. 2011; Kormendy & Ho 2013; Davis et al. 2017), we adopt the conventional form (Merritt 1999), where the stellar velocity dispersion of host SMBH mass M_{SMBH} is:

$$M_{\text{SMBH}} = 3.1 \times 10^8 M_{\odot} \left(\frac{\sigma_*}{200 \text{ km/s}} \right)^4. \quad (5)$$

This choice ensures that the dependence of the pre-existing BH maximum radius on the SMBH mass coincides with that of the AGN disk size (Eq. 30). The Keplerian speed can then be calculated by

$$v_{\text{kep}} = \sqrt{\frac{G(M_{\text{SMBH}} + M_{\text{c}})}{r}}, \quad (6)$$

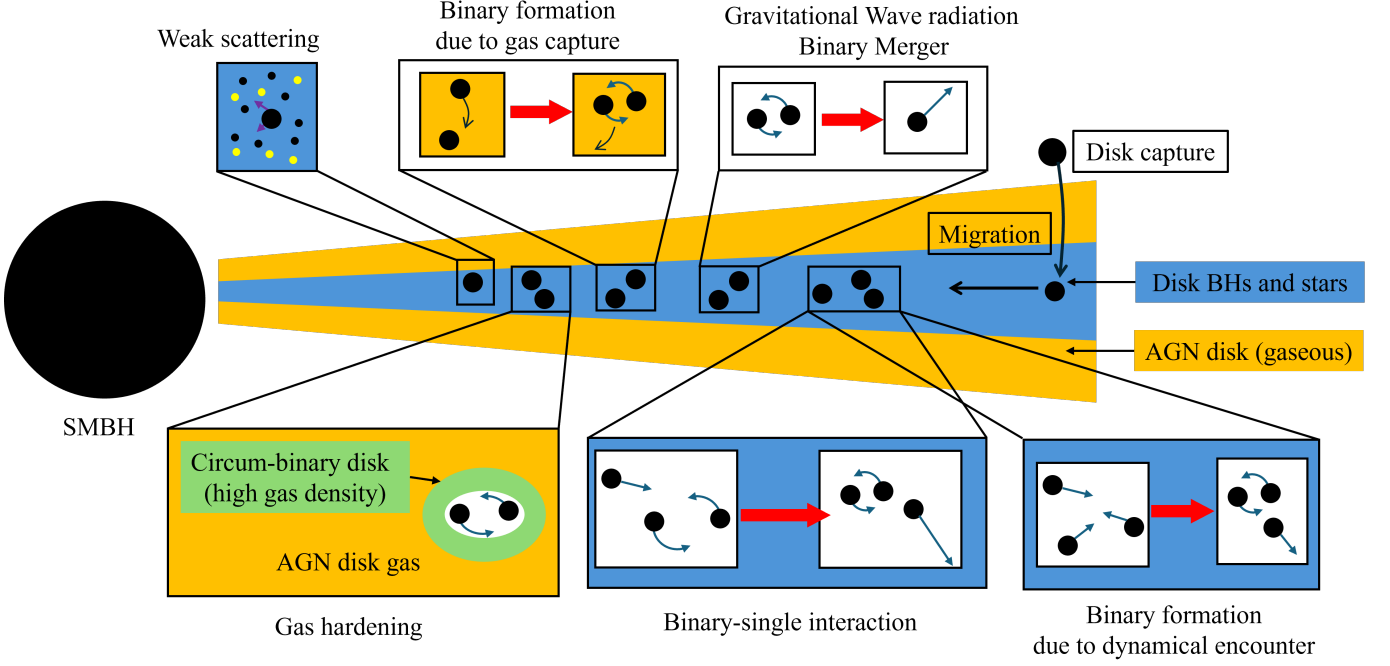


Figure 2. Schematic diagram illustrating the mechanisms incorporated in the program. The orange region represents the AGN disk, while the blue region denotes disk components (including both stars and BHs), which have a much smaller thickness compared to the AGN disk. All interaction types are depicted, though their positions are not drawn to scale.

where the enclosed mass $M_{<}$ is defined as:

$$M_{<}(r) = 4\pi \int_0^r dr' r'^2 \bar{m}_* n_*(r'). \quad (7)$$

In our fiducial model, the BH number density is given by:

$$n_{\text{BH}}(r) = \frac{N_{\text{BH,ini}}}{4\pi(r_{\text{BH,out}} - r_{\text{in}})^3} \left(\frac{r}{r_{\text{BH,out}} - r_{\text{in}}} \right)^{\gamma_p - 2}, \quad (8)$$

where the maximum BH distance to center $r_{\text{BH,out}}$ is set to be the same as the galactic nucleus size r_i (Eq. 3), and the total number of pre-existing BHs scales with SMBH mass fiducially as (Miralda-Escudé & Gould 2000):

$$N_{\text{BH,ini}} = 20000 \times \frac{M_{\text{SMBH}}}{4 \times 10^6 M_\odot}. \quad (9)$$

We select $M_{\text{SMBH}} = 4 \times 10^6 M_\odot$ as the default SMBH mass. As a comparison with Tagawa et al. (2020b), we also set a default stellar population for an SMBH mass of $4 \times 10^6 M_\odot$, where the stellar number density in Eq. 2 is replaced by:

$$n_*(r) = \left(\frac{M_{*,3\text{pc}}}{4.3 \bar{m}_*} \text{pc}^{-3} \right) \left(\frac{r}{0.3 \text{ pc}} \right)^{-0.5} \left[1 + \left(\frac{r}{0.3 \text{ pc}} \right)^4 \right]^{-0.325} \quad (10)$$

where $M_{*,3\text{pc}} = 10^7 M_\odot$ is the total stellar mass in 3 pc. The average stellar mass \bar{m}_* is calculated using initial mass function in Eq. 1 with index β_{IMF} , for the stellar mass m_* between $0.1 M_\odot$ and $20 M_\odot$.

We set the fraction f_{pre} as the ratio of pre-existing binaries to the total number of BH systems (single number + binary number), and adopt a fiducial value of $f_{\text{pre}} = 0.15$ following Tagawa et al. (2020b). The masses of the binary components, denoted as M_1 and M_2 , are generated independently through Eq. 1 and $M_{\text{BH}} = M_1 + M_2$ becomes the total mass of the binary. In our simulations, we treat a BH binary of mass M_1 and M_2 as a single BH of mass $M_{\text{BH}} = M_1 + M_2$. The binary separation s of pre-existing BH follows a log-flat distribution, ranging from $s_{\text{min}} = R_{*,1} + R_{*,2}$ to s_{max} , where $R_{*,1}$ and $R_{*,2}$ are the stellar radii of components 1 and 2, determined by their progenitor stellar masses (Torres et al. 2010):

$$R_* = R_\odot \left(\frac{m_s}{M_\odot} \right)^{1/2}. \quad (11)$$

We apply the relationship between BH mass and progenitor stellar mass in Tagawa et al. (2020b) as:

$$M_{\text{BH}} = \begin{cases} \frac{m_*}{4} & 20 \leq m_* < 40 \\ 10 & 40 \leq m_* < 55 \\ \frac{m_*}{13} + 5.77 & 55 \leq m_* < 120 \\ 15 & 120 \leq m_* < 140 \end{cases}. \quad (12)$$

The progenitor stellar mass is the inverse of Eq. 12 and generalized as $M_* = 13(M_{\text{BH}} - 15 M_\odot) + 140 M_\odot$ when $M_{\text{BH}} > 15 M_\odot$.

The maximum pre-existing BH separation $s_{\text{max}} = \max(R_{\text{max}}, s_{\text{bound}})$ is set to be the maximum value of $R_{\text{max}} =$

Type	Symbol	Description	Fiducial value	Plot range
simulation	N_{cell}	Number of radial cells in simulation	120	Convergence test
simulation	N_{mass}	Number of mass cells in background calculation	100	Convergence test
simulation	η_t	Time step	0.1	Convergence test
simulation	r_{in}	Inner bound of simulation	$r_{\text{disk,in}}$	Convergence test
simulation	r_{out}	Outer bound of simulation	$r_{\text{disk,out}}$	Convergence test
SMBH	M_{SMBH}	SMBH mass	$4 \times 10^6 M_{\odot}$	$10^5 - 10^9 M_{\odot}$
AGN disk	$r_{\text{disk,in}}$	Inner bound of AGN disk	10^{-4} pc, following Eq. 29	$0.5 \times 10^{-4} - 1.5 \times 10^{-4}$ pc
AGN disk	$r_{\text{disk,out}}$	Outer bound of AGN disk	5 pc, following Eq. 30	5 - 10 pc
AGN disk	\dot{M}_{out}	Accretion rate at the outer bound of AGN disk	$0.1 \dot{M}_{\text{Edd}}$	$0.025 \dot{M}_{\text{Edd}} - 0.20 \dot{M}_{\text{Edd}}$
AGN disk	ξ	Pressure ratio	1	no change due to instability
AGN disk	m_{AM}	Angular momentum transport rate	0.1	0.05 - 0.3
AGN disk	α_{SS}	Viscosity α parameter	0.1	0.05 - 0.25
AGN disk	ϵ	Conversion efficiency	10^{-4}	$10^{-4} - 10^{-3}$
AGN disk	t_{AGN}	AGN life time	10 Myr	10 - 100 Myr
AGN disk	$\beta_{\text{IMF,cre}}$	Star creation IMF index	2.35	1.7 - 2.35
Mass distribution	β_{IMF}	IMF index of pre-existing BH	2.35	1.7 - 2.35
Mass distribution	$M_{\text{BH,ini,min}}$	Minimum single BH mass of pre-existing BH	$5 M_{\odot}$	no change due to observational fact
Mass distribution	$M_{\text{BH,ini,max}}$	Maximum single BH mass of pre-existing BH	$15 M_{\odot}$	$15 - 30 M_{\odot}$
Radial distribution	γ_{ρ}	Index of radial distribution	0.0	-0.4 - 0.4
Radial distribution	$N_{\text{BH,ini}}$	Initial BH number in the AGN (within $r_{\text{BH,out}}$)	20000, following Eq. 9	20000 - 100000
Radial distribution	$r_{\text{BH,out}}$	Maximum BH radial distance to SMBH of pre-existing BH	following Eq. 3	2.5 - 3.5 pc
Velocity(inclination distribution)	β_v	Velocity dispersion parameter (Gaussian distribution only)	0.2	0.2 - 1.0
Binary	f_{pre}	Pre-existing binary BH fraction	0.15	0 - 0.2
Binary	R_{max}	Maximum separation of pre-existing binary BH	$10^5 R_{\odot}$	$10^4 - 10^5 R_{\odot}$
Gas interaction	f_{mig}	Migration factor	2.0	1.0 - 3.0
Gas interaction	$\ln \Lambda_{\text{gas}}$	Coulomb logarithm of gas dynamical friction	3.1	1.0 - 5.0
Gas interaction	Γ_{Edd}	Max accretion rate with respect to Eddington ratio	1	0.5 - 2
Gas interaction	η_c	Radiative efficiency	0.1	considered together using $\Gamma_{\text{Edd}}/(\eta_c/0.1)$

Table 1. Parameter List for all variables changed in the simulation. The fiducial values of the parameters except for the parameters plotted are applied to all simulations.

$10^5 R_\odot$ and the soft-hard boundary at distance r derived in Eq. 86, in case the soft binaries are usually breaks into singles due to the soft binary single interaction in Section 2.5.2.

The simulation also tracks the relative velocity with respect to the AGN disk's rotational (Keplerian) velocity as they cross the disk. The inclination angle i to the AGN disk is approximated with the z-components of relative speed, $\frac{v_z}{v_{\text{kep}}} = \sin i$. The x and y velocity relative to the v_x and v_y are generated in the same manner as v_z to save the computational cost. We investigate two basic inclination/dispersion models: (1) an isotropic model, where the BH position vector's direction and velocity's direction are both randomly distributed on a 2D sphere, and (2) a highly anisotropic Gaussian distribution of BH as in Tagawa et al. (2020b). In the isotropic model the inclination angle distribution follows:

$$\frac{dN}{di} = \frac{i}{2} \sin i. \quad (13)$$

In the anisotropic model $v_{x,y,z}/v_{\text{kep}}$ follow a normal distribution with a mean of 0 and dispersion β_v , as suggested by Tagawa et al. (2020b):

$$\frac{dN}{d \sin i} = \frac{1}{\sqrt{2\pi \left(\frac{\beta_v}{\sqrt{3}}\right)^2}} \exp \left[-\frac{\sin^2 i}{2 \left(\frac{\beta_v}{\sqrt{3}}\right)^2} \right]. \quad (14)$$

The rare occurrence of conditions of $\sin i > 1$ or $\sin i < -1$ indicates that the BHs are "free" and unbound from the SMBH. Additionally, a BH is also considered "free" if its relative velocity $v = \sqrt{v_x^2 + v_y^2 + v_z^2}$ exceeds $\sqrt{2}v_{\text{kep}}$. In such cases, the simulation for that BH is terminated.

For all subsequent discussions involving the inclination angle i , its negative counterpart $-i$ will automatically included, since the AGN disk structure and interactions are symmetric with respect to the disk (xy) plane. The fraction of the BHs with inclination $0 \leq i \leq i_0$ (also including $-i_0 \leq i \leq 0$) relative to the total number of BHs at radius r is then given by:

$$F(i_0) = \begin{cases} \text{erf} \left(\frac{\sqrt{3} \sin i_0}{\sqrt{2}\beta_v} \right) & \text{Gaussian} \\ \sin i_0 - i_0 \cos i_0 & \text{Isotropic} \end{cases}. \quad (15)$$

Figure 3 presents the cumulative density function (CDF) of the inclination distribution $F(i_0)$ from Eq. 15. The Gaussian distribution, regardless of β_v , exhibits a similar growth rate on a log scale, whereas the isotropic model starts with a low fraction at small inclinations before rising sharply. As a result, the number density of BHs captured by the AGN disk remains comparable across Gaussian models but is significantly lower for the isotropic model, which lead to a reduced merger rate. A higher disk BH density in the Gaussian model also increases the frequency of binary-single interactions and binary formation via gas capture, as discussed in Sec. 3.2.

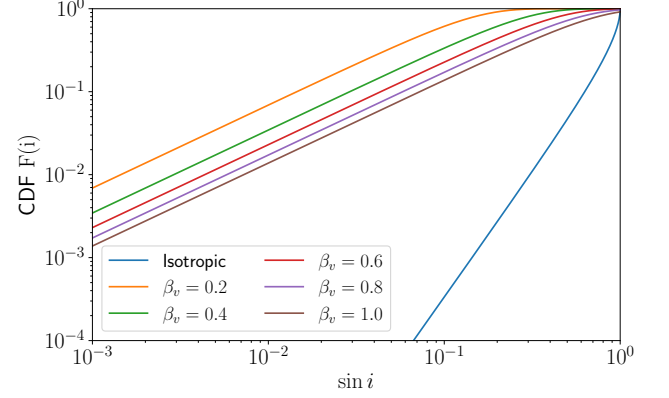


Figure 3. The cumulative density function (CDF) of the inclination distribution $F(i_0)$, as defined in Eq. 15. Compared to the isotropic model, the Gaussian distribution yields a significantly larger population of low-inclination pre-existing BHs, leading to a greater number of BHs falling into the disk gradually over time.

2.2. AGN disk model

We adopt the AGN disk model proposed by Thompson et al. (2005) and the Keplerian speed is modified by Eq. 6 as suggested by Tagawa et al. (2020b). We assume that the AGN disk rotates with Keplerian speed in the xy plane. Given the mass of the SMBH, M_{SMBH} , and assuming the disk velocity at radius r is the Kepler velocity $v_{\text{kep}}(r)$, the gas properties of an AGN disk at radius r are: gas density ρ , aspect ratio h/r , gas temperature T , effective temperature of radiation T_{eff} , the accretion rate \dot{M} , opacity $\kappa(\rho, T)$, the vertical optical depth τ_v , and the star formation rate $\dot{\Sigma}_*$. The Kepler speed determined by the stellar density (Eq. 6) will replace equation C1 in Thompson et al. (2005). Equations C2-C13 in Thompson et al. (2005) still apply. The equations to solve the properties are listed below:

$$\rho \frac{k_B}{m_p} T + \epsilon \dot{\Sigma}_* c \left(\frac{1}{2} \tau_v + \xi \right) = \rho \left(\frac{h}{r} \right)^2 v_{\text{kep}}^2 \quad (16)$$

$$T^4 = \frac{3}{4} T_{\text{eff}}^4 \left(\tau_v + \frac{4}{3} + \frac{2}{3\tau_v} \right) \quad (17)$$

$$\tau_v = \rho h \kappa(\rho, T) \quad (18)$$

$$\dot{M} = \dot{M}_{\text{out}} - \int_r^{r_{\text{disk,out}}} 2\pi r \dot{\Sigma}_* dr \quad (19)$$

$$\sigma_{\text{SB}} T_{\text{eff}}^4 = \frac{1}{2} \epsilon \dot{\Sigma}_* c^2 + \frac{3}{8\pi} \dot{M} \left(1 - \sqrt{\frac{r_{\text{disk,in}}}{r}} \right) \left(\frac{v_{\text{kep}}}{r} \right)^2, \quad (20)$$

where c is the speed of light, σ_{SB} is the Stefan-Boltzmann constant, k_B is the Boltzmann constant, m_p is the proton mass, r_{in} and r_{out} are the inner and outer boundary of the AGN disk.

We adopt the analytical Rosseland mean opacity model as described in Appendix A of Bell & Lin (1993). The accretion

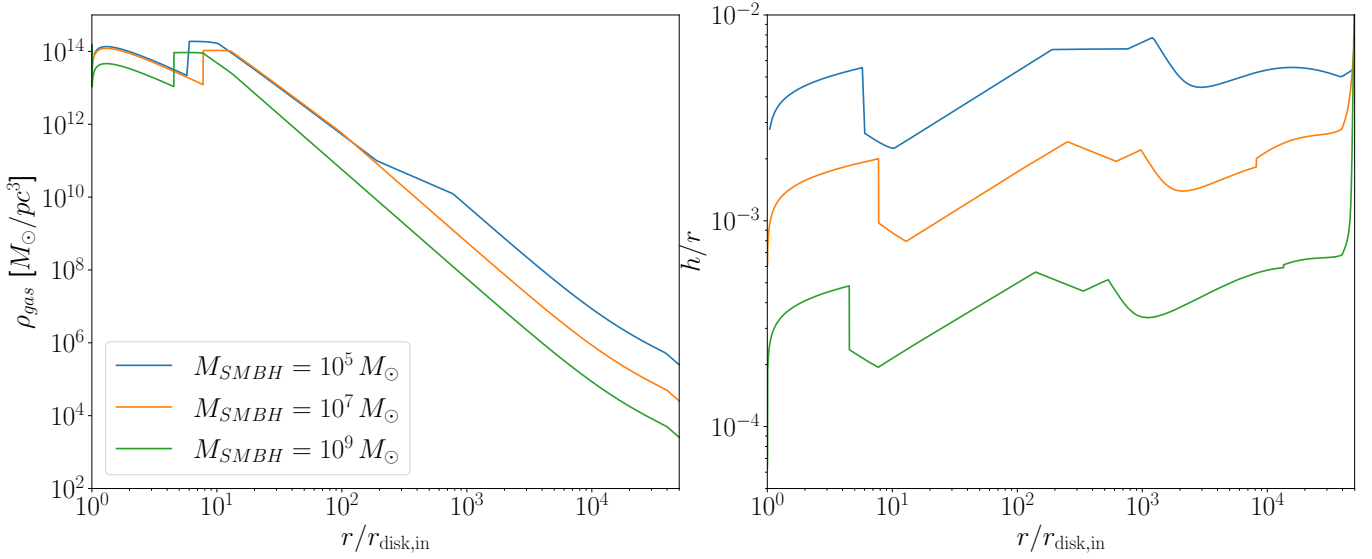


Figure 4. Example of gas density ρ (in M_\odot/pc^3) and aspect ratio h/r as functions of radius r in our fiducial model (n_s with Eq. 2). The blue, orange, and green curves correspond to the gas density or aspect ratio for host SMBH mass $10^5 M_\odot$, $10^7 M_\odot$, and $10^9 M_\odot$. The radius r is normalized by the inner radius of the disk (Eq. 29).

rate at the outer boundary, \dot{M}_{out} is selected to be a fraction of the Eddington accretion rate, with its fiducial value given by:

$$\frac{\dot{M}_{\text{out}}}{0.1\dot{M}_{\text{Edd}}} = 1, \quad (21)$$

where $\dot{M}_{\text{Edd}} = L_{\text{Edd}}(M_{\text{SMBH}})/(0.1c^2)$ is the Eddington accretion limit with radiation efficiency $\eta = 0.1$.

In the outer region, the accretion heat is insufficient to maintain Toomre parameter $Q = 1$ and thus the star formation rate is non zero. The Toomre parameter condition $Q = 1$ is thus equivalent to:

$$\rho = \frac{v_{\text{kep}}^2/r^2}{\sqrt{2}\pi G}. \quad (22)$$

Angular momentum transport is primarily driven by global torques, represented by a constant fraction m_{AM} :

$$\dot{M} = 4\pi r^2 \left(\frac{h}{r}\right)^2 \rho v_{\text{kep}} m_{\text{AM}}. \quad (23)$$

The parameters in the outer disk region are solved based on Eqs. 16–21, subject to the conditions outlined in Eqs. 22 & 23.

In the middle region, the accretion heat is sufficient to maintain $Q = 1$, resulting in the cessation of star formation. In this region, the degree of angular momentum transport m_{AM} is adjusted to ensure that the Toomre parameter remains $Q = 1$. The parameters in the middle region are then determined based on Eqs. 16–21, subject to conditions $\dot{\Sigma}_* = 0$ and Eq. 22.

In the inner region where $Q > 1$, the accretion is driven by a local viscosity, represented by

$$\dot{M} \left(1 - \sqrt{\frac{r_{\text{disk,in}}}{r}}\right) = 4\pi\alpha_{\text{ss}}\rho r^3 \left(\frac{h}{r}\right)^3 \frac{v_{\text{kep}}}{r} \left|\frac{d \ln \Omega}{d \ln r}\right|. \quad (24)$$

where α_{ss} is the α parameter of the Shakura-Sunyaev model, $\Omega = v_{\text{kep}}/r$ is the Keplerian angular velocity, and the factor $\left|\frac{d \ln \Omega}{d \ln r}\right|$ is given based on stellar density (Eq. 2),

$$\left|\frac{d \ln \Omega}{d \ln r}\right| = \left|\frac{3}{2} - \frac{G\bar{m}_* n_* r^2}{v_{\text{kep}}^2}\right|. \quad (25)$$

The parameters in the inner region are then determined based on Eqs. 16–21, with condition $\dot{\Sigma}_* = 0$ and Eq. 24. For simplicity we assume that, when $r = r_{\text{in}}$, all disk properties are 0.

For stars and BHs formed in the AGN disk, we adopt the model of Tagawa et al. (2020b), where the stars are formed following initial mass function with index β_{cre} between $m_{\text{s,min}} = 0.1M_\odot$ and $m_{\text{s,max}} = 140M_\odot$:

$$\frac{dN}{dm_*} = \mathcal{F}_{\text{cre}}(m_*, m_{\text{s,min}}, m_{\text{s,max}}) = \frac{(1 - \beta_{\text{cre}})m_*^{-\beta_{\text{cre}}}}{m_{\text{s,max}}^{1-\beta_{\text{cre}}} - m_{\text{s,min}}^{1-\beta_{\text{cre}}}}. \quad (26)$$

Stars of mass between $m_{*,\text{change}} = 20M_\odot$ and $m_{*,\text{max}} = 140M_\odot$ will become BHs immediately after they are formed. The mass of BHs follow the initial mass function of their progenitors and the relation in Eq. 12.

The conversion efficiency ϵ in Eqs. 16 and 20 represents the efficiency of converting the star formation rate into radiation. Thompson et al. (2005) assumes $\epsilon = 10^{-3}$ for a Salpeter IMF (Eq. 26) in the range $1 - 100M_\odot$, while

Tagawa et al. (2020b) and Epstein-Martin et al. (2025) suggests that ϵ may vary with AGN lifetime, stellar lifetime, and the star formation IMF index β_{cre} . Using the method outlined in Appendix A of Tagawa et al. (2020b), we estimate ϵ to range from 10^{-4} to 10^{-3} within our simulation parameters ($10 \text{ Myr} \leq t_{\text{AGN}} \leq 100 \text{ Myr}$, $1.7 \leq \beta_{\text{cre}} \leq 2.35$). In this paper, we treat ϵ as a free parameter independent of β_{cre} and t_{AGN} , setting a default value of 10^{-4} for $t_{\text{AGN}} = 10 \text{ Myr}$ and $\beta_{\text{cre}} = 2.35$.

We then denote following parameters: the average stellar mass $\bar{m}_{*,\text{cre}}$ for stars that are not BH progenitors, the average stellar mass $\bar{m}_{*,\text{change}}$ of BH progenitors, and the average BH mass $\bar{m}_{\text{BH},\text{cre}}$ from star formation. The mass fraction of BH progenitor stars, relative to the total stellar mass, is denoted as f_{BH} . The star and BH formation rates (number per area per time) can be expressed as follows:

$$\left(\frac{dN_{\text{BH}}}{dA dt} \right)_{\text{cre}} = \frac{f_{\text{BH}} \dot{\Sigma}_*}{\bar{m}_{\text{change}}}, \quad (27)$$

$$\left(\frac{dN_*}{dA dt} \right)_{\text{cre}} = \frac{(1 - f_{\text{BH}}) \dot{\Sigma}_*}{\bar{m}_*}. \quad (28)$$

We compute the average number of BHs formed within the AGN lifetime, assuming their formation times are uniformly distributed between 0 and t_{AGN} . The masses of the newly formed BHs are randomly generated according to the initial mass function in Eqs. 26 and 12. The velocities relative to AGN disk are assumed to be the sound speed, given by $\vec{v} = c_s \hat{n}$ where \hat{n} is a random 3D unit vector. For simplicity, we assume that the binary fraction of star formation is consistent with that of the background pre-existing BHs.

In a disk where the outer boundary $r_{\text{disk,out}}$ exceeds our simulation range r_{out} , we can effectively consider an AGN disk of $r_{\text{disk,out}} = r_{\text{out}}$ with a much lower accretion rate than normal outer boundary accretion rate as $\dot{M}_{5\text{pc}}/(0.1\dot{M}_{\text{Edd}}) < 1$. Changes in the disk size can thus be accounted for by adjustments in the accretion rate at r_{out} , which may result in significant orders of magnitude changes $\dot{M}_{5\text{pc}}/(0.1\dot{M}_{\text{Edd}}) \ll 1.0$. In our default settings, the size of the disk is scaled similarly to the AGN size, as given by Eq. 3, in relation to the SMBH mass. Specifically, we define the outer boundaries of the disk proportional to $\sqrt{M_{\text{SMBH}}}$, motivated by Mid-IR observations (Burtscher et al. 2013). For simplicity, we assume that the inner boundaries scale the same way as the outer boundaries:

$$r_{\text{disk,in}} = 10^{-4} \text{ pc} \left(\frac{M_{\text{SMBH}}}{4 \times 10^6 M_{\odot}} \right)^{1/2}, \quad (29)$$

$$r_{\text{disk,out}} = 5 \text{ pc} \left(\frac{M_{\text{SMBH}}}{4 \times 10^6 M_{\odot}} \right)^{1/2}. \quad (30)$$

In reality, the inner radius of the AGN disk is expected to be smaller than the value given by Eq. 29. In the model by Thompson et al. (2005), the equations governing the inner

region (Eqs. 16-21, $\dot{\Sigma}_* = 0$ and Eq. 24) fail to yield solutions near the radius $r_{\text{disk,in}}$ (e.g. $r_{\text{disk,in}} = 6GM_{\text{SMBH}}/c^2 = r_{\text{ISCO}}$). To avoid this issue and effectively analyze the impact of migration traps in the AGN disk, we adopt a larger $r_{\text{disk,in}}$ in Eq. 29, which ensures that the impact of the migration trap becomes more pronounced, as discussed in section 2.4.3 below.

In Eq. 19, the AGN accretion rate decreases rapidly, and thus the number of cells needs to be increased to avoid a negative accretion rate. In this way, the number of (log scale) radius steps is thus determined by Eq. 19:

$$\Delta(\ln r)_{\text{max}} = \frac{0.01 \dot{M}_{\text{out}}}{2\pi r_{\text{disk,out}}^2 \dot{\Sigma}_*(r_{\text{disk,out}})} \quad (31)$$

$$N_{\text{disk}} = \left\lceil \ln \left(\frac{r_{\text{disk,out}}}{r_{\text{disk,in}}} \right) / \Delta(\ln r)_{\text{max}} \right\rceil + 1 \quad (32)$$

The disk properties are converted into values at standard grid boundary and cell center (determined by N_{cell}) in the next step.

In Figure 4, we illustrate how the gas density ρ and the aspect ratio h/r changes with the radius. The gas density ρ decreases slightly as the SMBH mass increases, with radii rescaled to $r_{\text{disk,in}}$ (left panel), while h/r decreases correspondingly (right panel). Notably, the aspect ratio h/r remains approximately constant for a given SMBH mass, which implies that the initial inclination of objects entering the disk is largely independent of radius. Both the gas density and disk thickness are critical factors in determining the number of BHs within the disk, as they directly affect the disk's capacity to capture and retain BHs within its structure. The variations in gas density and aspect ratio in the AGN disk, influenced by different host SMBH masses, lead to complex effects on the physical processes discussed in later sections.

2.3. Gravitational interaction

2.3.1. Gravitational wave radiation

Gravitational radiation gradually hardens binary systems through energy loss. Using the gravitational-wave hardening rate for a binary with zero eccentricity from Peters (1964), we express this rate as:

$$\Gamma_{\text{GW}} = -\frac{(ds/dt)_{\text{GW}}}{s} = \frac{64 G^3 M_1 M_2 (M_1 + M_2)}{5 c^5 s^4}, \quad (33)$$

where M_1 and M_2 are the masses of the primary and secondary BHs in the binary system.

2.3.2. Merger prescription

We assume that the BH binary merges and forms a new remnant single BH when the separation of the BH binary reaches the innermost stable circular orbit $r_{\text{ISCO}} = 6GM_{\text{BH}}/c^2$. The newly formed BH experiences a recoil

due to anisotropic gravitational-wave emission and undergoes mass loss from GW radiation. We adopt the model used in Tagawa et al. (2020b) and neglect the effect of spin and mass ratio, the single mass (Tichy & Marronetti 2008) and velocity after merger is then described by:

$$M_{\text{BH, single}} = M_{\text{BH}} \left[1 - \frac{q}{5(1+q)^2} \right], \quad (34)$$

$$\vec{v}_{\text{single}} = \vec{v}_{\text{bin}} + v_{\text{GW}} \left[\frac{q^2(1-q)}{(1+q)^5} \right] \hat{n}, \quad (35)$$

where \hat{n} is a random 3D vector and $v_{\text{GW}} = 8830 \text{ km/s}$ (Baker et al. 2007).

2.4. Gas interaction

Each BH crosses the AGN disk twice per orbital period, interacting with the gas on both occasions. Although the relative velocity of the BH varies during each crossing, we use the same relative velocity in simulations to reduce computational costs. This is justified since the eccentricity of BH orbits is typically close to zero. A BH is considered to be fully embedded in the disk when its orbital height is smaller than the disk's half-thickness $h_z = r \frac{|v_z|}{v_{\text{kep}}} < h$. The ratio of time the BH spends within the disk per orbit period, denoted as p_{disk} is given by:

$$p_{\text{disk}} = \begin{cases} 1 & \text{BH resides in the disk} \\ \frac{2}{\pi} \arcsin \left[\left(\frac{h}{r} \right) / \left(\frac{|v_z|}{v_{\text{kep}}} \right) \right] & \text{BH is outside the disk} \end{cases}. \quad (36)$$

When a BH is inside the disk, the angular momentum flux from the BH locally dominates the viscous flux due to a large mass difference from stellar mass BH and SMBH. As a consequence, the torque it exerts depletes the surrounding gas density, forming a gap at its radius, in which the surface density is smaller than its unperturbed value. When the BH is outside the disk, we neglect the angular momentum flux injected into the disk as it is small compared to the transport of angular momentum due to the disk. As a result, the gas density remains approximately unperturbed. We approximate the gas density around the BH suggested by Kanagawa et al. (2018) as:

$$\rho_{\text{gas}} = \begin{cases} \rho / (1 + 0.04K) & \text{BH resides in the disk} \\ \rho & \text{BH is outside the disk} \end{cases}, \quad (37)$$

where the dimensionless factor K considering the local disk angular momentum transport is given by:

$$K = \left(\frac{M_{\text{BH}}}{M_{\text{SMBH}}} \right)^2 \left(\frac{h}{r} \right)^{-5} \alpha_{\text{eff}}^{-1}. \quad (38)$$

The effective α parameter α_{eff} , is calculated through out the simulation range by replacing α_{SS} with α_{eff} in Eq. 24. In the inner region of AGN disk $\alpha_{\text{eff}} = \alpha_{\text{SS}}$ while in other regions $\alpha_{\text{eff}} > \alpha_{\text{SS}}$.

2.4.1. Accretion

We assume that the gas within the Bondi-Hoyle-Lyttleton (BHL) radius is interacting with the BH. The BHL radius is defined as:

$$r_{\text{BHL}} = \frac{GM_{\text{BH}}}{(c_s^2 + v^2)}. \quad (39)$$

where c_s is the sound speed of the gas and v is the relative velocity between the BH and the AGN disk. The rescaled Bondi-Hoyle-Lyttleton accretion rate is:

$$\Gamma_{\text{acc}} = \frac{\dot{m}_{\text{BHL}}}{M_{\text{BH}}} = \frac{4\pi r_w r_h \rho_{\text{gas}} (c_s^2 + v^2)^{1/2}}{M_{\text{BH}}} \quad (40)$$

where

$$r_{\text{Hill}} = r \left(\frac{M}{3M_{\text{SMBH}}} \right)^{1/3}, \quad (41)$$

$$r_w = \min(r_{\text{BHL}}, r_{\text{Hill}}, r_{\text{shear}}), \quad (42)$$

$$r_h = \min(r_w, h), \quad (43)$$

$$r_{\text{shear}} = \frac{GM_{\text{BH}}}{(r_{\text{Hill}} v_{\text{kep}}/r)^2}. \quad (44)$$

The relative velocity of the BH to the gas decreases at a rate:

$$\frac{d\vec{v}}{dt} = -\Gamma_{\text{acc}} p_{\text{disk}} \vec{v}, \quad (45)$$

where p_{disk} is the ratio of time the BH spends in the disk every orbit period.

The mass of the BH increases but is limited by the Eddington rate. The default Eddington limit is given by $\dot{M}_{\text{Edd}}(M_{\text{BH}}) = L_{\text{Edd}}(M_{\text{BH}})/(0.1c^2)$, where L_{Edd} is the Eddington luminosity and the fiducial radiation efficiency is set to $\eta_c = 0.1$. The BH mass increases as:

$$\frac{dM_{\text{BH}}}{dt} = \min \left(M_{\text{BH}} \Gamma_{\text{acc}} p_{\text{disk}}, \frac{\Gamma_{\text{Edd}}}{\eta_c/0.1} \dot{M}_{\text{Edd}}(M_{\text{BH}}) \right). \quad (46)$$

Here $\Gamma_{\text{Edd}} = 1$ is the fiducial Eddington ratio of stellar mass BHs. To investigate the impact of accretion, we vary $\Gamma_{\text{Edd}}/(\eta_c/0.1)$, which effectively alters both the accretion limit and the radiation efficiency η_c .

For binary BHs, the total mass $M_{\text{BH}} = M_1 + M_2$ is used to compute the mass increase (also applicable to gas dynamical friction and migration). The component masses should change as follows:

$$\frac{dM_2}{dt} = \min \left(\frac{\lambda}{1+\lambda} \Gamma_{\text{acc}} M_{\text{BH}} p_{\text{disk}}, \frac{\Gamma_{\text{Edd}}}{\eta_c/0.1} \dot{M}_{\text{Edd}}(M_2) \right) \quad (47)$$

$$\frac{dM_1}{dt} = \min \left(M_{\text{BH}} \Gamma_{\text{acc}} p_{\text{disk}} - \frac{dM_2}{dt}, \frac{\Gamma_{\text{Edd}}}{\eta_c/0.1} \dot{M}_{\text{Edd}}(M_1) \right) \quad (48)$$

where λ is a dimensionless function of mass ratio q , given by equation (1) in Kelley et al. (2019).

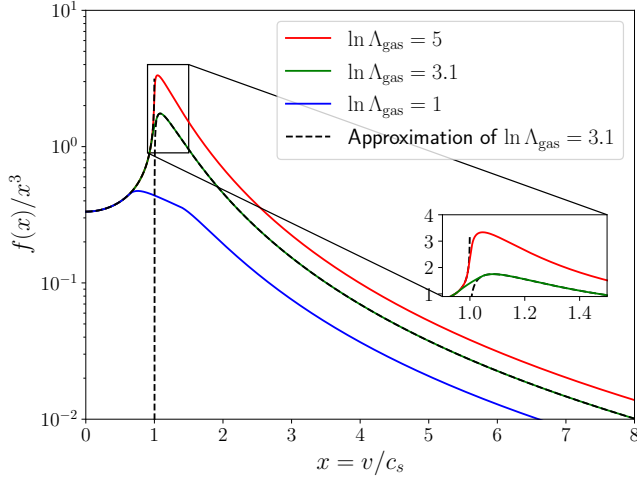


Figure 5. The gas dynamical friction factor $f(x)/x^3$ at different $x = v/c_s$ for $\ln \Lambda_{\text{gas}} = 1$ (blue), 3.1 (fiducial value, green), and 5 (red). The singularity of the approximation (dashed black) is removed at $x = 1$, and the peak of this function is at $x \sim 1.1$ that varies slightly due to $\ln \Lambda_{\text{gas}}$.

2.4.2. Gas dynamical friction

We adopt the formulation of [Ostriker \(1999\)](#) for the deceleration of a BH with a non-zero relative velocity to the gaseous disk. The deceleration rate due to gas dynamical friction (GDF) is given by

$$\Gamma_{\text{GDF}} = -\frac{(dv/dt)_{\text{GDF}}}{v} = \frac{4\pi G^2 M_{\text{BH}} \rho_{\text{gas}}}{c_s^3} \frac{f(x)}{x^3}, \quad (49)$$

where $x = v/c_s$, and we can analytically integrate $f(x)$ in [Ostriker \(1999\)](#) and assume the $\ln \Lambda_{\text{gas}} = -\ln x_m = \ln \frac{c_s t}{r_{\text{min}}}$ in the formula, then

$$f(x) = \begin{cases} \frac{1}{2} \ln \left(\frac{1+x}{1-x} \right) - x & x < 1 - x_m \\ \frac{1}{2} \ln \left(\frac{1+x}{x_m} \right) + \frac{(x-x_m)^2 - 1}{4x_m} & 1 - x_m \leq x < 1 + x_m \\ \frac{1}{2} \ln(x^2 - 1) + \ln \Lambda_{\text{gas}} & x \geq 1 + x_m \end{cases} \quad (50)$$

We adopted a Coulomb logarithm for gas $\ln \Lambda_{\text{gas}} = 3.1$ as the fiducial value suggested by [Chapon et al. \(2013\)](#). Compared to the approximation used in [Tagawa et al. \(2020b\)](#), we remove the singularity at $v = c_s$, which occurs when the BH orbits near the AGN disk, as shown in the Fig. 5. When a BH is outside but near the disk $i \sim h/r$, the gas dynamical friction reaches the maximum and it helps the BH rapidly fall into the disk. When a BH has a large inclination, its relative velocity is very large compared to the sound speed, leading to a low dynamical friction rate $\Gamma_{\text{GDF}} \sim \ln x/x^3$. Additionally, we approximate the formula for very low velocities $v \ll c_s$:

$$\Gamma_{\text{GDF}} = \frac{4\pi G^2 M_{\text{BH}} \rho_{\text{gas}}}{3c_s^3} + \mathcal{O}(x). \quad (51)$$

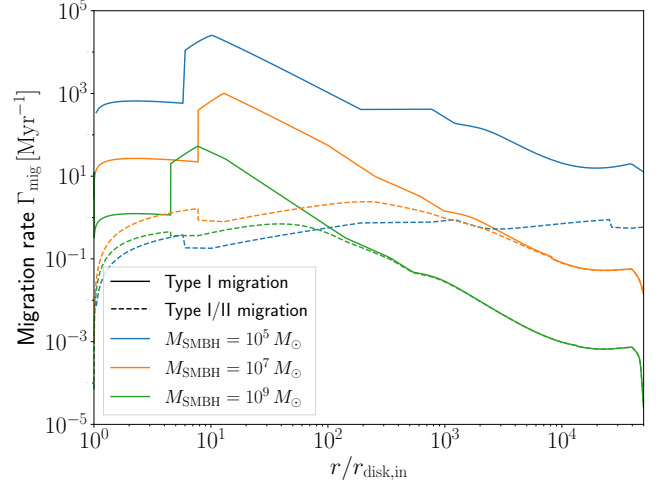


Figure 6. Migration rate of a $10M_{\odot}$ test BH as a function of radius for different SMBH masses. The radius is normalized by the inner disk radius $r_{\text{disk,in}}$ (Eq. 29). The solid lines represent the Type I migration rate, while the dashed lines show the Type I/II migration rate, accounting for gap opening in the disk.

The gas dynamical friction disappears when the Bondi-Hoyle-Lyttleton radius is smaller than the size of the H II sphere ([Park & Bogdanović 2017](#)). The condition can be rewritten as ([Tagawa et al. 2020b](#)):

$$\left(\frac{\rho_{\text{gas}}}{2m_{\text{gas}} \times 10^{14} \text{ m}^{-3}} \right) \left(\frac{M_{\text{BH}}}{10M_{\odot}} \right) \left(\frac{v}{10 \text{ km/s}} \right)^{-3} > 1, \quad (52)$$

where the average atomic mass of gas is $m_{\text{gas}} = (1 - Y_{\text{He}})m_{\text{H}} + Y_{\text{He}}m_{\text{He}}$ and we adopt the default Helium mass fraction $Y_{\text{He}} = 0.24$ as suggested by [Dors et al. \(2022\)](#). The gas dynamical friction recovers when $v > 50 \text{ km/s}$ as suggested by [Park & Bogdanović \(2017\)](#) and [Park & Ricotti \(2013\)](#).

2.4.3. Migration

In the studies of protoplanetary disks ([Tanaka et al. 2002; Ward 1997; Goldreich & Tremaine 1979](#)), the Lindblad resonances between a low-mass planet and the surrounding gas lead to a loss of angular momentum. This process results in radial migration, known as Type I migration. When a planet becomes sufficiently massive, it repels the surrounding gas due to nonlinear torques, creating a density gap along its orbital path, which is known as Type II migration. Similar migration behavior also applies to the interaction between BHs or stars and an AGN disk, as discussed by [Bellovary et al. \(2016\)](#). In particular, the conditions for Type II migration is not hard to be satisfied ($K \gtrsim 25$) in our AGN disk models when BHs reside in the disk.

For simplicity, we adopt the same formula in [Tagawa et al. \(2020b\)](#), accounting for both Type I and II migration with the reduced gas in the gap ([Kanagawa et al. 2018](#)):

$$\Gamma_{\text{mig}} = 2f_{\text{mig}} \left(\frac{M_{\text{BH}}}{M_{\text{SMBH}}} \right) \left(\frac{2\rho_{\text{gas}} r^2 v_{\text{kep}}}{M_{\text{SMBH}}} \right) \left(\frac{h}{r} \right)^{-1}, \quad (53)$$

where ρ_{gas} is the perturbed gas density profile discussed in Eq. 37, and f_{mig} is a dimensionless parameter that quantifies the strength of the migration effect. In particular, the dimensionless factor f_{mig} is approximately 2.0 but generally varies depending on the local disk properties, (Tanaka et al. 2002; Paardekooper et al. 2010; Baruteau et al. 2011). We treat f_{mig} as a free parameter to assess its impact on merger rate and merger mass.

Fig. 6 illustrates the dependence of the migration rate on the SMBH mass. The Type I migration rate, which applies to BHs outside the AGN disk, follows a similar trend as the gas density profile and approximately scales with M/M_{SMBH} as in Eq. 53. For BHs embedded in the AGN disk, the combined Type I/II migration is suppressed in the inner region due to gap opening (Eq. 37), maintaining a similar order of magnitude for all SMBH mass. In the outer region, where BHs are generally too light to open gaps (except for very low SMBH masses, e.g., $M_{\text{SMBH}} = 10^5 M_{\odot}$), the migration rate converges with Type I migration and remains lower. A deceleration in migration velocity occurs around $r \sim 10r_{\text{disk,in}}$ due to a discontinuity in the gas density, effectively forming a discontinuous migration trap (Bellovary et al. 2016). The details of migration traps will be discussed in Section 4.3.

2.4.4. Binary hardening due to gas interaction

The analytical formulation of gas-driven binary hardening remains uncertain. In our model, a 2D circum-binary disk may form around the binary, exhibiting a higher gas density than its surroundings (Fig. 2). Therefore, both gas dynamical friction and the torque exerted by the circum-binary disk contribute to the binary hardening process:

$$\Gamma_{\text{gas},s} = -\frac{(ds/dt)_{\text{gas}}}{s} = \Gamma_{\text{GDF},s} + \Gamma_{\text{CBD},s} \quad (54)$$

Many simulation studies (Baruteau et al. 2010; Li et al. 2022; Rowan et al. 2023) confirm that gravitational drag dominates over gas accretion effects, leading to merger timescales much shorter than the AGN disk lifetime, as illustrated in Fig. 8. For simplicity, we do not distinguish between prograde and retrograde binaries, despite their hardening rate differences (Li & Lai 2022).

We adopt gas dynamical friction for the gas hardening timescale following Eq. (49), with the feedback condition given by Eq. 52 or for $v > 50$ km/s:

$$\Gamma_{\text{GDF},s} = \frac{4\pi G^2 M_{\text{BH}} \rho_{\text{gas}}}{c_s^3} \frac{f(x)}{x^3}, \quad x = \frac{\sqrt{GM_{\text{BH}}/s}}{c_s}. \quad (55)$$

Here, the relative speed is approximated as the binary's orbital velocity $\sqrt{GM_{\text{BH}}/s}$, the gas density is taken as the gap density ρ_{gas} , and the sound speed c_s corresponds to that of the AGN disk. At large radii, where the gas density is lower, feedback effect generally stops gas dynamical friction when

the binary separation is large. In contrast, in the dense inner regions of the disk, the critical velocity defined by the feedback condition Eq. 52 can exceed 50 km/s, and gas dynamical friction remains effective throughout the hardening process.

We adopt the gas hardening formalism by Ishibashi & Gröbner (2020) for prograde binaries to evaluate the viscous interaction with circum-binary disk, assuming eccentricity $e = 0$. The circum-binary disk hardening rate is then:

$$\Gamma_{\text{CBD},s} = \frac{24\pi(1+q)^2 \alpha_{\text{CBD}} c_{s,\text{CBD}}^2 \Sigma_{\text{gas,CBD}}}{qM\omega}, \quad (56)$$

where $\omega = \sqrt{GM_{\text{BH}}/s^3}$ is the Keplerian angular velocity of the binary, and the subscript CBD denotes the value of circum-binary disk.

The properties of the circum-binary disk are calculated using Eqs. 5-14 from Haiman et al. (2009). We assume a gas-dominated disk in the inner region, with the viscous α parameter for circum-binary disk set to be $\alpha_{\text{CBD}} = 0.1$ as the fiducial value. The reduced accretion rate factor $\frac{\dot{m}}{\eta_c/0.1}$ is then given by Eq. 46:

$$\frac{\dot{m}}{\eta_c/0.1} = \frac{dM_{\text{BH}}/dt}{\dot{M}_{\text{Edd}}(M_{\text{BH}})} = \min\left(\Gamma_{\text{acc}} \frac{M_{\text{BH}}}{\dot{M}_{\text{Edd}}}, \frac{\Gamma_{\text{Edd}}}{\eta_c/0.1}\right). \quad (57)$$

The surface gas density of the circum-binary disk, Σ_{CBD} , is then given by:

$$\Sigma_{\text{CBD}} = 3.464 \times 10^8 \text{ g/cm}^2 \left(\frac{\dot{m}}{\eta_c/0.1}\right)^{3/5} \left(\frac{\alpha_{\text{CBD}}}{0.3}\right)^{-4/5} \left(\frac{M_{\text{BH}}}{M_{\odot}}\right)^{1/5} \left(\frac{s}{10^3 R_S}\right)^{-3/5} \quad \text{if } s < s_{\text{es/ff}}, \quad (58)$$

$$\Sigma_{\text{CBD}} = 2.388 \times 10^6 \text{ g/cm}^2 \left(\frac{\dot{m}}{\eta_c/0.1}\right)^{7/10} \left(\frac{\alpha_{\text{CBD}}}{3/10}\right)^{-4/5} \left(\frac{M_{\text{BH}}}{M_{\odot}}\right)^{1/5} \left(\frac{s}{10^3 R_S}\right)^{-3/4} \quad \text{if } s > s_{\text{es/ff}}, \quad (59)$$

and the aspect ratio of circum-binary disk $(h/r)_{\text{CBD}} = h_{\text{CBD}}/s$ is given by:

$$\left(\frac{h}{r}\right)_{\text{CBD}} = 7.5 \times 10^{-3} \dot{m} \left(\frac{s}{10^3 R_S}\right)^{-1} \quad \text{if } s < s_{\text{gas/rad}} \quad , \quad (60)$$

$$\left(\frac{h}{r}\right)_{\text{CBD}} = 1.019 \times 10^{-2} \left(\frac{\dot{m}}{\eta_c/0.1}\right)^{1/5} \left(\frac{\alpha_{\text{CBD}}}{0.3}\right)^{-1/10} \left(\frac{M_{\text{BH}}}{M_\odot}\right)^{-1/10} \left(\frac{s}{10^3 R_S}\right)^{1/20} \quad \text{if } s_{\text{gas/rad}} < s < s_{\text{es/ff}} \quad , \quad (61)$$

$$\left(\frac{h}{r}\right)_{\text{CBD}} = 6.121 \times 10^{-3} \left(\frac{\dot{m}}{\eta_c/0.1}\right)^{3/20} \left(\frac{\alpha_{\text{CBD}}}{0.3}\right)^{-1/10} \left(\frac{M_{\text{BH}}}{M_\odot}\right)^{-1/10} \left(\frac{s}{10^3 R_S}\right)^{1/8} \quad \text{if } s > s_{\text{es/ff}} \quad . \quad (62)$$

The separation of transition between inner region and middle region $s_{\text{gas/rad}}$ and between middle region and outer region $s_{\text{es/ff}}$ are given by:

$$\frac{s_{\text{gas/rad}}}{R_S} = 0.104 \left(\frac{\dot{m}}{\eta_c/0.1}\right)^{16/21} \left(\frac{\alpha_{\text{CBD}}}{0.3}\right)^{2/21} \left(\frac{M_{\text{BH}}}{M_\odot}\right)^{2/21} \quad (63)$$

$$\frac{s_{\text{es/ff}}}{R_S} = 4.10 \times 10^3 \left(\frac{\dot{m}}{\eta_c/0.1}\right)^{2/3} \quad (64)$$

In practice, if the circum-binary disk gas density $\rho_{\text{CBD}} = \Sigma_{\text{CBD}}/(2h_{\text{CBD}})$ is lower than the gap gas density ρ_{gas} , we assume that the circum-binary disk does not form, where the $\Sigma_{\text{gas,CBD}}$ in Eq. 56 is assumed to be 0.

2.5. Interaction between stars and BHs

BHs interact with objects in their surroundings, which alters their velocity, and can result in binary formation or the change of binary separation. We consider the interaction between the main BH (or BH binary) and three types of surrounding components (denoted with subscript c): spherical background stars (back), BHs in the AGN disk (DBH), and stars in the AGN disk (Ds). For each component type, we calculate four key parameters: the average mass m_c , the average local number density n_c , the average velocity dispersion relative to disk velocity σ_c , and the average scale height h_c . Note that $\sigma_c = 0$ indicates that the component co-rotates with the disk. We assume that the fraction of time a BH or BH binary interacts with a given component, p_c corresponds to the fraction of time it remains within the scale height of that component.

We treat the spherical background stellar component (denoted with subscript back) as a static background that does not evolve over time. Any BH will always interact with the

spherical stars. The spherical background stellar properties are then:

$$(m_{\text{back}}, n_{\text{back}}, \sigma_c, h_{\text{back}}) = \left(\bar{m}_*, n_*(r), \frac{v_{\text{kep}}(r)}{\sqrt{3}}, \frac{r}{\sqrt{2}}\right) \quad (65)$$

$$p_{\text{back}} = 1 \quad (66)$$

The number density and average mass of disk components ($m_{\text{DBH}}, n_{\text{DBH}}, m_{\text{Ds}}, n_{\text{Ds}}$) are pre-calculated at the background level in Section 2.6. We assume that the velocity dispersion and the scale height of the disk components are identical, i.e., $\sigma_{\text{DBH}} = \sigma_{\text{Ds}}, h_{\text{DBH}} = h_{\text{Ds}}$. These values are derived in Section 2.6.2, and recalculated during each loop of the individual sample simulations. The ratio of time that a BH or BH binary interacts with disk components p_c is

$$p_c = \begin{cases} 1 & \frac{h_c}{r} \geq \frac{|v_z|}{v_{\text{kep}}} \\ \frac{2}{\pi} \arcsin \left[\left(\frac{h_c}{r}\right) / \left(\frac{|v_z|}{v_{\text{kep}}}\right) \right] & \frac{h_c}{r} < \frac{|v_z|}{v_{\text{kep}}} \end{cases} \quad (67)$$

In this scenario, we assume that all interactions between an individual sample (a single BH or BH binary) and the surrounding components occur within the Hill radius r_{Hill} . At this distance, the relative speed between the binary and the surrounding components, v_{rel} , is then calculated as:

$$v_{\text{rel}} = \max(\sqrt{3}\sigma_c, v, v_{\text{rel,mig}}, v_{\text{shear}}), \quad (68)$$

where the relative migration velocity is $v_{\text{rel,mig}} = (\Gamma_{\text{mig}} - \Gamma_{\text{mig,c}})r$. The migration rate of spherical background stars is set to be $\Gamma_{\text{mig,back}} = 0$, and the migration rate of the disk components is computed using Eq. 53 with average mass m_c . The shear velocity between the BH sample and the 3rd object from component is

$$v_{\text{shear}} = p_{\text{uni}} r_{\text{Hill}} \frac{v_{\text{kep}}}{r}. \quad (69)$$

where p_{uni} is uniform between 0 and 1.

When analyzing the interaction between individual samples and disk BH components, we account for the fact that binary formation depletes the population of single BHs at approximately the same radii. To reflect this, we adjust the number density of disk BHs as follows:

$$n_{\text{DBH,int}} = \max\left(n_{\text{DBH}} - \frac{N_{\text{form}}}{V_{\text{DBH}}}, 0\right), \quad (70)$$

where n_{DBH} is calculated in section 2.6 as an evolving background, N_{form} represents the number of binaries formed within the cell (which resets to zero once the BH migrates to a different cell), and V_{DBH} is the volume of the disk BH population within the cell, given by:

$$V_{\text{DBH}} = \pi(r_{\text{right}}^2 - r_{\text{left}}^2)h_{\text{DBH}}, \quad (71)$$

where r_{left} and r_{right} is the right left bound radii of the radial grid.

As a result, the modified number density, $n_{\text{DBH,int}}$, which is applied to interactions with disk BH components, effectively suppresses binary formation and binary-single interactions at small radii. This mechanism naturally limits the formation of new binaries as the available population of single BHs is depleted.

We define the impact parameter for a 90° deflection angle due to gravity as b_{90} :

$$b_{90} = \frac{G(M_{\text{BH}} + m_c)}{v_{\text{rel}}^2}, \quad (72)$$

where v_{rel} is the relative velocity between the BH and the surrounding object.

When discussing the interactions between other components (denote by subscript c), the scale height is modified as:

$$h_{\text{eff}} = \max\left(\frac{|v_z|}{v_{\text{kep}}} \cdot r, h_c\right). \quad (73)$$

2.5.1. Weak scattering

A weak interaction refers to the velocity exchange resulting from encounters between BH and its surrounding objects. According to the Fokker-Planck approximation in [Binney & Tremaine \(2011\)](#), the change in velocity due to weak scattering, $\Delta \vec{v}_{\text{WS}}$, consists of a dynamical friction term $\Delta \vec{v}_{\text{DF}}$ and a diffusion term $\Delta \vec{v}_{\text{diffusion}}$. The change of the velocity in time Δt using Monte Carlo method is:

$$\Delta v_{\text{DF}} = p_c D[\Delta v_{\parallel}] \Delta t, \quad (74)$$

$$\Delta v_{\text{diffusion}} = p_c \sqrt{D[\Delta v_{\perp}^2] + D[\Delta v_{\parallel}^2]} \Delta t, \quad (75)$$

$$\Delta \vec{v}_{\text{WS}} = \Delta v_{\text{DF}} \hat{v} + \Delta v_{\text{diffusion}} \hat{n}, \quad (76)$$

where \hat{v} is the unit vector of velocity direction, \hat{n} is a random 3D vector.

When the impact parameter is smaller than the scale height of the surrounding components, $b_{90} < h_c$, we apply the weak scattering approximation for an infinite homogeneous medium (Equation 7.92 in [Binney & Tremaine \(2011\)](#)). The Coulomb logarithm Λ_{WS} is set to be $\Lambda_{\text{WS}} = h_c/b_{90}$, suggested by [Papaloizou & Larwood \(2000\)](#), and the mass density of the surrounding component is $\rho_c = n_c m_c$. The dynamical friction and diffusion coefficients of velocity change are then given by:

$$D[\Delta v_{\parallel}] = -\frac{4\pi G^2 (M_{\text{BH}} + m_c) m_c n_c \ln \Lambda_{\text{WS}}}{\sigma_c^2} G(X), \quad (77)$$

$$D[\Delta v_{\perp}^2] = \frac{4\pi \sqrt{2} G^2 m_c n_c \ln \Lambda_{\text{WS}}}{\sigma_c} \frac{G(X)}{X}, \quad (78)$$

$$D[\Delta v_{\perp}^2] = \frac{4\pi \sqrt{2} G^2 m_c n_c \ln \Lambda_{\text{WS}}}{\sigma_c} \left[\frac{\text{erf}(X) - G(X)}{X} \right]. \quad (79)$$

The quantity $X = |\vec{v} - \vec{v}_c|/(\sqrt{2}\sigma_c)$, where $v_c = 0$ for disk components since they co-rotate with disk with low dispersion, and $v_c = v_{\text{kep}}$ for spherical component. The function $G(x)$ is given by:

$$G(X) = \frac{1}{2X^2} \left[\text{erf}(X) - \frac{2X}{\sqrt{\pi}} e^{-X^2} \right]. \quad (80)$$

When the impact parameter is larger than the scale height of the surrounding components, $b_{90} \geq h_c$, the scattering angle is less than 90 degrees, and the dynamical friction and diffusion terms are confined to two dimensions. The modified diffusion terms are (Appendix B of [Tagawa et al. \(2020b\)](#)):

$$D[\Delta v_{\parallel}] = \begin{cases} 0 & c=\text{DBH \& Ds} \\ -9.765 G m_c n_c h_c & c=\text{back} \end{cases}, \quad (81)$$

$$D[\Delta v_{\parallel}^2] = D[\Delta v_{\perp}^2] = \begin{cases} (2\pi)^{3/2} G m_c n_c h_c \frac{\sigma_c m_c}{M_{\text{BH}} + m_c} & c=\text{DBH \& Ds} \\ 12.7 G m_c n_c h_c \frac{\sigma_c m_c}{M_{\text{BH}} + m_c} & c=\text{back} \end{cases}. \quad (82)$$

where the \hat{n} in Eq. 76 becomes a random vector in the xy plane.

2.5.2. Binary single interaction

Binary BHs sometimes undergo significant changes in their separation when interacting with surrounding objects, e.g. [Binney & Tremaine \(2011\)](#). These interactions are characterized by close gravitational interactions between the binary and a third object. The cross-section for these encounters is approximated as $\sigma_{\text{coll}} = b_{xy} b_z$, where the effective impact parameters in the xy plane (disk plane) and z direction b_{xy} and b_z are given by:

$$b_{xy} = \min\left(s \sqrt{1 + \frac{2b_{90}}{s}}, r_{\text{Hill}}\right), \quad (83)$$

$$b_z = \min(b_{xy}, h_{\text{eff}}). \quad (84)$$

The rate of binary-single interactions for the component c , denoted as $\Gamma_{\text{BS},c}$, is given by:

$$\Gamma_{\text{BS},c} = p_c n_c \sigma_{\text{coll}} v_{\text{rel}}. \quad (85)$$

The probability of a BH undergoing a binary-single interaction within time Δt is $\Gamma_{\text{BS},c} \Delta t$.

Binary-single interactions can be classified into two regimes based on the comparison between the binary's binding energy and the kinetic energy of the surrounding objects. When the binary's binding energy $E_b = GM_1 M_2 / (2s)$ is smaller than the kinetic energy of the surrounding objects $E_c = \frac{3}{2} m_c \sigma_c^2 / 2$, the binary is "soft" and experiences a softening interaction, primarily relevant for encounters with background stars. The soft-hard boundary separation is given by:

$$s_{\text{soft,hard}} = \frac{G m_1 m_2}{3 m_{\text{back}} \sigma_{\text{back}}^2} = \frac{q}{(1+q)^2} \frac{G M_{\text{BH}}^2}{\bar{m}_s v_{\text{kep}}^2}, \quad (86)$$

Initially, pre-existing binary separations must be smaller than the soft-hard boundary, as wide binaries are destroyed before AGN disk formation. The softening rate applied to the BH binary is derived in [Gould \(1991\)](#):

$$\left(\frac{ds}{dt}\right)_{\text{BS,back}} = \frac{16}{3} \frac{Gn_{\text{back}}m_{\text{back}}s^2}{M_{\text{BH}}\sigma_{\text{back}}^3} (E_b - E_c) \ln\left(\frac{GM_{\text{BH}}}{s\sigma_{\text{back}}^2}\right). \quad (87)$$

Conversely, "hard" binaries, where the binding energy exceeds the kinetic energy of the surrounding objects, undergo hardening ([Leigh et al. 2018](#)). This process is common in interactions with disk components due to their low velocity dispersion, resulting from significant dynamical friction. The total energy of the system, consisting of the binary BH and the surrounding object, is determined by:

$$E_0 = \frac{1}{2} \frac{m_c M_{\text{BH}}}{m_c + M_{\text{BH}}} v_{\text{rel}}^2 - \frac{GM_{\text{BH}}m_c}{r_{\text{Hill}}} - E_b. \quad (88)$$

We choose the escape velocity from [Leigh et al. \(2018\)](#) to estimate the velocity change of the main object Δv_{BH} , since it is typically smaller than the binary velocity $v_{\text{bin}} = (GM_1M_2/s)^{1/2}$. The recoil velocity after the interaction is described by:

$$\Delta \vec{v}_{\text{BH}} = \vec{v}_{\text{recoil}} = \alpha \left[\frac{M_{\text{BH}}}{m_c(m_c + M_{\text{BH}})} |E_0| \right]^{1/2} \hat{n}, \quad (89)$$

and the separation hardening rate is:

$$E_{b,f} = E_b + \frac{\alpha^2}{2} |E_0|. \quad (90)$$

$$s_f = \frac{GM_1M_2}{2E_{b,f}} \quad (91)$$

$$\left(\frac{ds}{dt}\right)_{\text{BS}} = \frac{s_f - s_i}{\Delta t}. \quad (92)$$

2.5.3. Binary Formation due to Three-body Interaction

In dense or low-velocity dispersion regions, a close encounter of three objects can result in binary formation (e.g., [Binney & Tremaine 2011](#)). The encounter impact parameter is constrained by the gravitational interaction and is selected as:

$$b_i = \min(b_{90}, r_{\text{Hill}}). \quad (93)$$

The vertical (z-direction) extent of the disk, combined with the component scale height, further limits the impact parameters, such that the effective vertical impact parameter becomes $b_{z,\text{eff}} = \min(b_i, h_{\text{eff}})$. The mean rate of a two-body encounter is given by $\Gamma_2 = p_c n_c b_i b_{z,\text{eff}} v_{\text{rel}}$, where the third object must be located within a volume of $b_i^2 b_z$, with $b_z = \min(b_i, h_c)$. This leads to the three-body encounter rate ([Tagawa et al. 2020b](#)):

$$\Gamma_{3bbf} = p_{\text{DBH}} n_{\text{DBH}} \left(\frac{1}{2} n_{\text{DBH}} + n_{\text{Ds}} \right) b_i^3 b_{z,\text{eff}} b_z v_{\text{rel}}. \quad (94)$$

The factor 1/2 on disk BH number density accounts for the double counting effect, and the 3rd object could potentially be the disk stars instead of BHs. The probability of a three-body encounter resulting in binary formation within time Δt is $P = \Gamma_{3bbf} \Delta t$. The binary that forms from such an interaction will have the following properties:

$$M_{\text{bin}} = M_{\text{BH}} + m_{\text{BH},2} \quad (95)$$

$$\vec{v}_{\text{bin}} = \vec{v}_{\text{kick}} + \vec{v}_{\text{cen}} \quad (96)$$

$$s_{\text{bin}} = b_i \quad (97)$$

where the kick velocity is

$$\vec{v}_{\text{kick}} = \frac{m_c}{M_{\text{BH}} + m_{\text{BH},2} + m_c} \sqrt{\frac{GM_{\text{BH}}m_{\text{BH},2}}{b_i}}, \quad (98)$$

and the center-of-mass velocity is

$$\vec{v}_{\text{cen}} = \frac{M_{\text{BH}}\vec{v}_{\text{BH}} + m_{\text{BH},2}\vec{v}_2 + m_c\sigma_{\text{DBH}}\hat{n}_2}{M_{\text{BH}}m_{\text{BH},2} + m_c}. \quad (99)$$

The partner BH of this binary formation is chosen directly from the pre-existing BH at the same cell. The mass $m_{\text{BH},2}$ and velocity \vec{v}_2 are generated from Eq. 1 and inclination in Eq. 14.

2.5.4. Binary formation via gas capture

In AGN disks, a binary may form if sufficient energy is dissipated during the interaction of two BHs. Gas dynamical friction is the primary mechanism responsible for dissipating energy in such encounters near the disk ([DeLaurentiis et al. 2023](#)). [Qian et al. \(2024\)](#) also considers a gravitational wave-assisted formation channel for close encounters with an impact parameter of $\sim 2 \times 10^{-5} r_{\text{Hill}}$. More recent studies ([Rowan et al. 2024a,b](#)) provide refined predictions for separation, eccentricity, and encounter rates. To optimize computational efficiency, we adopt the formalism from [Goldreich et al. \(2002\)](#) and [Tagawa et al. \(2020b\)](#), where the fraction of binding energy lost during a passage through the mutual Hill sphere is proportional to the fraction of time that two bodies remain within this Hill radius. The timescale for crossing the Hill radius is:

$$t_{\text{pass}} = \frac{r_{\text{Hill}}}{v_{\text{rel},c}}, \quad (100)$$

The gas dynamical friction rate, $\Gamma_{\text{GDF}}(v_{\text{rel},c})$, reduces the relative velocity between the two bodies during this interaction following Eq. 49. The probability of binary formation due to gas capture during a single encounter is:

$$P_{\text{cap}} = \min(1, \Gamma_{\text{GDF}} t_{\text{pass}}). \quad (101)$$

The rate of BH encounters with disk BH components is ([Tagawa et al. 2020b](#)):

$$\Gamma_{\text{enc}} = n_{\text{DBH}} r_{\text{Hill}} \bar{z}_{\text{Hill}} v_{\text{rel}} p_{\text{DBH}}, \quad (102)$$

where

$$z_{\text{Hill}} = \min(r_{\text{Hill}}, h_{\text{DBH}}). \quad (103)$$

The gas capture rate of a single BH is then:

$$\Gamma_{\text{cap}} = \Gamma_{\text{enc}} P_{\text{cap}}. \quad (104)$$

Thus, the probability of gas capture during a time step Δt is $P = \Gamma_{\text{cap}} \Delta t$. When a gas capture event occurs, it is assumed to happen within the AGN disk, where gas dynamical friction remains effective. The BH binary properties are given by

$$M_{\text{bin}} = M_{\text{BH}} + m_{\text{BH},2}, \quad (105)$$

$$\vec{v}_{\text{bin}} = \vec{v}_{\text{BH}}, \quad (106)$$

$$s_{\text{bin}} = r_{\text{Hill}}, \quad (107)$$

where in our simulation, the mass of the partner BH is assumed to be $m_{\text{BH},2} = m_{\text{DBH}}(r, t)$.

2.6. Statistical Background

2.6.1. Number density and average mass

The surface distribution of disk BHs is characterized as:

$$\frac{dN_{\text{DBH}}}{(2\pi r dr) dM} = \Sigma(r, M). \quad (108)$$

We then obtain the maximum disk BH distribution, assuming that all BHs at r fall into the disk without radial migration:

$$\Sigma_{\text{max}}(r, M) = 2rn_{\text{BH}}(r)\mathcal{F}_{\text{pre}}(M), \quad (109)$$

where the $\mathcal{F}_{\text{pre}}(M)$ is the Salpeter initial mass function in Eq. 1. The initial surface distribution of disk BHs is only a fraction of the maximum surface density, scaled by the function $F(i_{\text{disk}})$ (Eq. 15). The initial inclination at the disk surface, i_{disk} —which also corresponds to the inclination at time $t = 0$ when AGN disk is formed—is defined as:

$$i_{\text{disk}} = i_{\text{ini}}(t = 0) = \arcsin\left(\frac{h}{r}\right) \quad (110)$$

Accordingly, the initial surface density distribution is expressed as:

$$\Sigma(t = 0, r, M) = \Sigma_{\text{max}}(r, M)F(i_{\text{disk}}). \quad (111)$$

The distribution of disk BHs evolves according to the following equation:

$$\begin{aligned} & \frac{1}{r} \left[\frac{\partial(r\Sigma(t, r, M))}{\partial t} + \frac{\partial(r\Sigma(t, r, M))}{\partial r} \frac{dr}{dt} + \frac{\partial(r\Sigma(t, r, M))}{\partial M} \frac{dM}{dt} \right] \\ &= \frac{dN_{\text{fall}}}{dAdt dM} + \left(\frac{dN_{\text{BH}}}{dAdt} \right)_{\text{cre}} \mathcal{F}(M). \end{aligned} \quad (112)$$

Here $\frac{dr}{dt} = -\Gamma_{\text{mig}} r$ and $\frac{dM}{dt} = \min(\Gamma_{\text{acc}} M, \frac{\Gamma_{\text{Edd}}}{\eta_c/0.1} \dot{M}_{\text{Edd}}(M))$ represent the migration and accretion effect in the disk, with

rate Γ_{mig} and Γ_{acc} defined in Eqs. 53 and 40. The term $\frac{dN_{\text{fall}}}{dAdt}$ represents the rate at which BHs fall from outside the disk, while $\left(\frac{dN_{\text{BH}}}{dAdt} \right)_{\text{cre}}$ denotes the BH formation rate within the disk in Eq. 27. The function $\mathcal{F}(M)$ is the normalized IMF for BHs formed due to star formation governed by β_{cre} , stellar creation function \mathcal{F}_{cre} and star-BH relation Eq. 12. In our timescale calculations, we assume that the velocity of the BH relative to the AGN disk is zero, as it is typically small compared to the sound speed, c_s . Additionally, we do not consider the formation of binary systems from single BHs in disk component calculation. The effect of these assumptions will be discussed in Sec. 4.2.

The number of time steps $\Delta t = t_{\text{AGN}}/N_{\text{time}}$ syncretizing this equation is then given by:

$$N_{\text{time}} = \left\lceil t_{\text{AGN}} / \left(0.01 / \max(\Gamma_{\text{mig}}, \Gamma_{\text{acc}}) \right) \right\rceil, \quad (113)$$

To evaluate the rate of BHs that fall into the AGN disk, we consider a BH of mass M_{BH} that enters the disk (inclination angle decrease to i_{disk}) at time t_0 . The BH initially has mass M_{ini} and inclination angle i_{ini} . The BH relative velocity to disk should evolve as

$$\frac{d\vec{v}}{dt} = -\vec{v}(\Gamma_{\text{acc}} + \Gamma_{\text{GDF}})p_{\text{disk}}(i). \quad (114)$$

Assuming a circular orbit, the relative velocity to the disk is given by $v = 2v_{\text{kep}} \sin \frac{i}{2}$, and the evolution of the BH's mass and inclination then follows:

$$\frac{dM_{\text{BH}}}{dt} = M_{\text{BH}} \cdot \max\left(\Gamma_{\text{acc}} p_{\text{disk}}, \frac{\Gamma_{\text{Edd}} L_{\text{Edd}}(M_{\text{BH}})}{M_{\text{BH}} \eta_c c^2}\right), \quad (115)$$

$$\frac{di}{dt} = -2 \tan \frac{i}{2} (\Gamma_{\text{acc}} + \Gamma_{\text{GDF}}) p_{\text{disk}}(i). \quad (116)$$

The gas dynamical friction rate Γ_{GDF} and accretion rate Γ_{acc} are calculated by Eqs. 49 and 40, and the time fraction $p_{\text{disk}}(i)$ is calculated by Eq. 36. Note that if the BH with initial mass M_{ini} and initial inclination i_{ini} enters the disk at time t , BH with same mass M_{ini} and inclination in range $-i_{\text{ini}} \leq i \leq i_{\text{ini}}$ should be all in the disk. The rate at which BHs fall into the disk is given by:

$$\begin{aligned} r \frac{dN_{\text{fall}}}{dAdt dM} &= r \frac{\Sigma_{\text{max}}(r, M_{\text{ini}}(t + \Delta t)) F(i_{\text{ini}}(t + \Delta t))}{\Delta t} \\ &\quad - r \frac{\Sigma_{\text{max}}(r, M_{\text{ini}}(t)) F(i_{\text{ini}}(t))}{\Delta t} \\ &= r \frac{d[\Sigma_{\text{max}}(r, M_{\text{ini}}) F(i_{\text{ini}})]}{dt}. \end{aligned} \quad (117)$$

The time steps in Eq. 117 is set to be $\Delta t = t_{\text{AGN}}/N_{\text{time}}$, consistent with Eq. 112. The values $i_{\text{ini}}(t + \Delta t)$ and $M_{\text{ini}}(t + \Delta t)$ can be computed directly from Eqs. 115 and 116 using initial conditions $i_{\text{ini}}(t)$ and $M_{\text{ini}}(t)$ and evolving over time Δt .

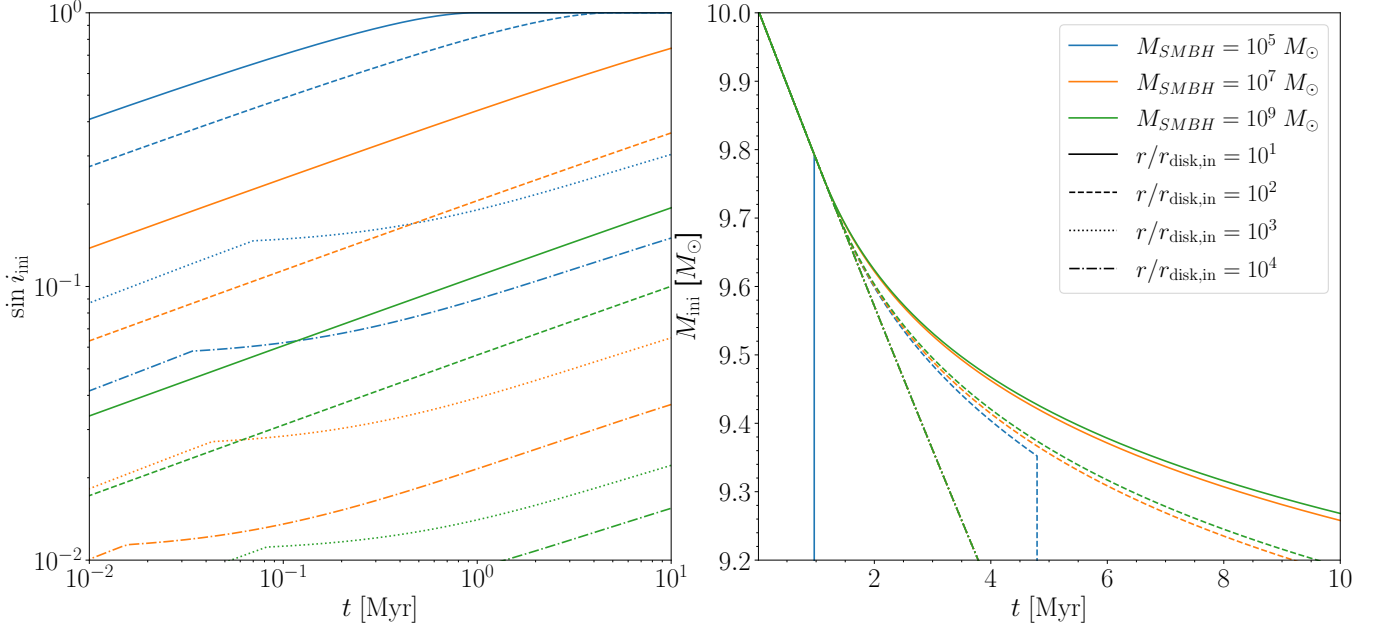


Figure 7. Initial inclination (left) and initial mass (right) as functions of falling time t of a BH mass $10M_{\odot}$ at different radii. The solid, dashed, dotted, and dash-dotted lines refer to the BHs falling into disk at radius $r/r_{\text{disk, in}} = 10^1, 10^2, 10^3, 10^4$. The red, blue, and green lines correspond to the host SMBH mass of $10^5, 10^7$, and $10^9 M_{\odot}$.

Fig. 7 illustrates the evolution of the initial inclination i_{ini} and initial mass M_{ini} as functions of the BH infall time t . On a log-log scale, the growth of $\sin i_{\text{ini}}$ appears nearly linear, slowing only when gas dynamical friction becomes ineffective in specific velocity regimes due to radiation feedback (Eq. 52). The initial inclination angle $i_{\text{ini}}(t = 0)$ is comparable to the disk aspect ratio h/r . It then increases rapidly over a short timescale (e.g. $\lesssim 10^{-2}$ Myr) due to the strong dynamical friction near the disk.

BHs around more massive SMBHs start at lower initial inclinations but increase at a nearly identical rate on a logarithmic scale (e.g., $M_{\text{SMBH}} = 10^9 M_{\odot}$, shown by the green line). Due to the lower gas density at larger radii, most disk BHs originate with small inclination angles (i.e. $\sin i_{\text{ini}} \sim O(10^{-2}) - O(10^{-1})$) and remain near the disk for an extended time. As a result, the mass gained through accretion becomes more significant at larger radii, as shown in the right panel Fig. 7. The vertical line in the right panel indicates the point at which mass accretion ceases, as all BHs have reached the disk within the given time frame. The initial mass shows minimal variation across different SMBH masses, attributed to their similar gas density profiles.

We neglect the migration of BHs outside the disk in this step to reduce computational cost. The surface number density and average mass of disk BHs at time t and radial dis-

tance r is then:

$$\Sigma_{\text{DBH}} = \int_{M_{\text{min}}}^{M_{\text{max}}} dM \Sigma(t, r, M), \quad (118)$$

$$m_{\text{DBH}} = \frac{\int_{M_{\text{min}}}^{M_{\text{max}}} dM M \Sigma(t, r, M)}{\int_{M_{\text{min}}}^{M_{\text{max}}} dM \Sigma(t, r, M)}. \quad (119)$$

The required disk BH number density n_{DBH} should be calculated by:

$$n_{\text{DBH}} = \Sigma_{\text{DBH}} / (2h_{\text{DBH}}), \quad (120)$$

where h_{DBH} is the scale height of disk BH in Eq. 124, determined by weak scattering process, as discussed in the section 2.6.2.

Using the discretization method from Section 2, we estimate the average mass and number density of disk BHs at any time within the AGN lifetime. The disk star average mass is set to be $m_{\text{Ds}} = \bar{m}_*$, while the number density of disk stars is calculated similarly. We do not account for the dynamical friction of stars, and the accretion of stars is assumed to proceed at the maximum Bondi-Hoyle-Lyttleton rate. We adopt Equation 11 of Bartos et al. (2017) as the timescale of the accretion rate of stars:

$$r_{\text{BHL},*}(i) = \frac{2G\bar{m}_*}{v_{\text{kep}}^2 \left[4 \sin^2 \frac{i}{2} + \left(\frac{h}{r} \right)^2 \right]}, \quad (121)$$

$$t_*(i) = \frac{\pi r}{v_{\text{kep}}} \frac{\bar{m}_* \cos \frac{i}{2}}{\rho \pi r \left(\frac{h}{r} \right) r_{\text{BHL},*}^2}. \quad (122)$$

The maximum initial inclination of disk stars at time t is solved via $t = t_*(i_{*,\text{ini}})$, and the number density of the disk stars is then

$$n_{Ds}(t) = \left[n_*(1 - \cos i_{*,\text{ini}}) + \frac{1}{r} \left(\frac{dN_*}{dAdt} \right)_{\text{cre}} \right] / \left(2 \frac{h_{Ds}}{r} \right). \quad (123)$$

2.6.2. Velocity dispersion and scale height

We assume that the disk star component has the same velocity dispersion and scale height as the disk BH component. As an approximation, the scale height of the disk component is estimated using the velocity dispersion σ_{DBH} :

$$h_{Ds} = h_{\text{DBH}} = \frac{\sigma_{\text{DBH}}}{v_{\text{kep}}} r. \quad (124)$$

The velocity dispersion of the disk component is taken to be the average velocity in the x, y and z components of the BH's relative velocity in the disk, with $v \sim \sqrt{3}\sigma_{\text{DBH}}$. We assume that the velocity dispersion represents the root mean square velocity in each component for a disk BH with mass m_{DBH} . When a BH falls into the disk, the z component of velocity $v_z = \left(\frac{h}{r}\right)v_{\text{kep}} = c_s$. At this point, the gas dynamical friction is near its maximum since $v \gtrsim c_s$. The dynamical friction rapidly reduces the velocity, resulting in $\sigma_{\text{DBH}} \ll c_s$. This effect continues to reduce the velocity until equilibrium is reached between the dominant gas dynamical friction, which drives the velocity decrease, and weak scattering diffusion. To capture this process, we use the leading-order term of gas dynamical friction rate in Eq. 51 and set the velocity change rate equal to the diffusion velocity as described in Eq. 75,

$$\sqrt{\left(D[\Delta v_\perp^2] + D[\Delta v_\parallel^2] \right)_c} \Delta t = \Gamma_{\text{GDF}} \sigma_{\text{DBH}} \Delta t. \quad (125)$$

The relative velocity of a Disk BH relative to background stellar component is determined by $\sqrt{3}\sigma_{\text{back}} = v_{\text{kep}}$ as the other terms are too small. Thus the impact parameter for 90-degree deflection is $b_{90} = G(m_{\text{back}} + m_{\text{DBH}})/v_{\text{kep}}^2$. Consequently, the Coulomb logarithm for weak scattering is given by:

$$\Lambda_{\text{WS}} = \left[\frac{\sqrt{2}G(m_{ss} + m_{\text{DBH}})}{rv_{\text{kep}}^2} \right]^{-1} \sim \frac{M_{\text{SMBH}}}{m_{ss} + m_{\text{DBH}}} \gg 1. \quad (126)$$

X is taken to be $\sqrt{3}/2$ in Eqs. 78 and 79 due to the low velocity of disk BHs, and the time interval is chosen to be $1/\Gamma_{\text{GDF}}$, the velocity dispersion is thus:

$$\sigma_{\text{DBH}} = 4.93 \sqrt{\frac{G^2 m_{\text{back}} n_{\text{back}} \ln \Lambda_{\text{WS}}}{v_{\text{kep}} \Gamma_{\text{GDF}}}}. \quad (127)$$

The disk BH and star components share the same velocity dispersion, and the relative velocity between two disk BHs

is small, leading to $\Lambda_{\text{WS}} < 1$. The diffusion velocity from disk components is thus only on the x - y plane and does not affect the scale-height. We neglect its effect on velocity dispersion and thus the velocity dispersion is slightly underestimated. The velocity dispersion of disk component is normally $\sim 10^{-3}c_s$ at outer region of AGN disk and $\sim 10^{-2}c_s$ at the inner region of AGN disk ($r \lesssim 10r_{\text{disk,in}}$).

2.7. Time step and evolution in individual BH simulation

In simulations of individual BHs, the number density and mass density of disk BHs is pre-calculated at the background level (Section 2.6.1) with time step $t_{\text{AGN}}/N_{\text{time}}$ (Eq. 113). We calculate the disk components' velocity dispersion σ_{DBH} and scale height h_{DBH} in each loop (Section 2.6.2), and then all the timescales of interactions with gas and stellar components. The time step of an individual BH simulation is then determined by:

$$\Delta t = \eta_t / \max(\Gamma_{\text{mig}} p_{\text{disk}}, \Gamma_{\text{acc}} p_{\text{disk}}, \Gamma_{\text{gas},s}, \Gamma_{\text{GW}}, \Gamma_{\text{BS},c} p_c), \quad (128)$$

where $\eta_t = 0.1$ as the default value and subscript c denotes the spherical background, disk BH and disk star components. The gas dynamical friction rate is very large near or in the disk, as shown in Figure 5. We thus neglect the gas dynamical friction term in the time step to reduce the computational cost.

The properties are updated in each time step as

$$r_{\text{new}} = r(1 - \Delta t \cdot \Gamma_{\text{mig}} p_{\text{disk}}), \quad (129)$$

$$s_{\text{new}} = s(1 - \Delta t \cdot \Gamma_{\text{gas},s})(1 - \Delta t \cdot \Gamma_{\text{GW}}) + \Delta t \cdot \sum_c \left(\frac{ds}{dt} \right)_{\text{BS}}, \quad (130)$$

$$\vec{v}_{\text{new}} = \vec{v} \cdot \exp(-\Gamma_{\text{GDF}} \Delta t p_{\text{disk}})(1 - \Gamma_{\text{acc}} \Delta t p_{\text{disk}}) + \sum_c \Delta \vec{v}_{\text{WS}} + \sum_c (\vec{v}_{\text{rec}})_{\text{BS}}, \quad (131)$$

$$M_{\text{new}} = M + \left(\frac{dM}{dt} \right)_{\text{acc}}. \quad (132)$$

To ensure consistency with the velocity dispersion calculation in Section 2.6.2, we set the time interval Δt_{WS} in Eqs. 74 and 75 as $\Delta t_{\text{WS}} = \min(\Delta t, 1/\Gamma_{\text{GDF}}/p_{\text{disk}})$.

3. RESULTS

3.1. Life of black hole binaries

We illustrate the interaction rate of binary or single BHs in Figure 8. For this analysis, we use SMBH mass $4 \times 10^6 M_\odot$, with the background disk parameters evaluated at $t = 3$ Myr, adopting a Gaussian inclination distribution with $\beta_v = 0.2$. The single BH mass is set to $10M_\odot$, while the BH binary mass two BHs is set to $10M_\odot + 10M_\odot$. The single and binary BHs are assumed to move at relative velocities $v_{x,y,z} = 10^{-3}c_s/\sqrt{3}$

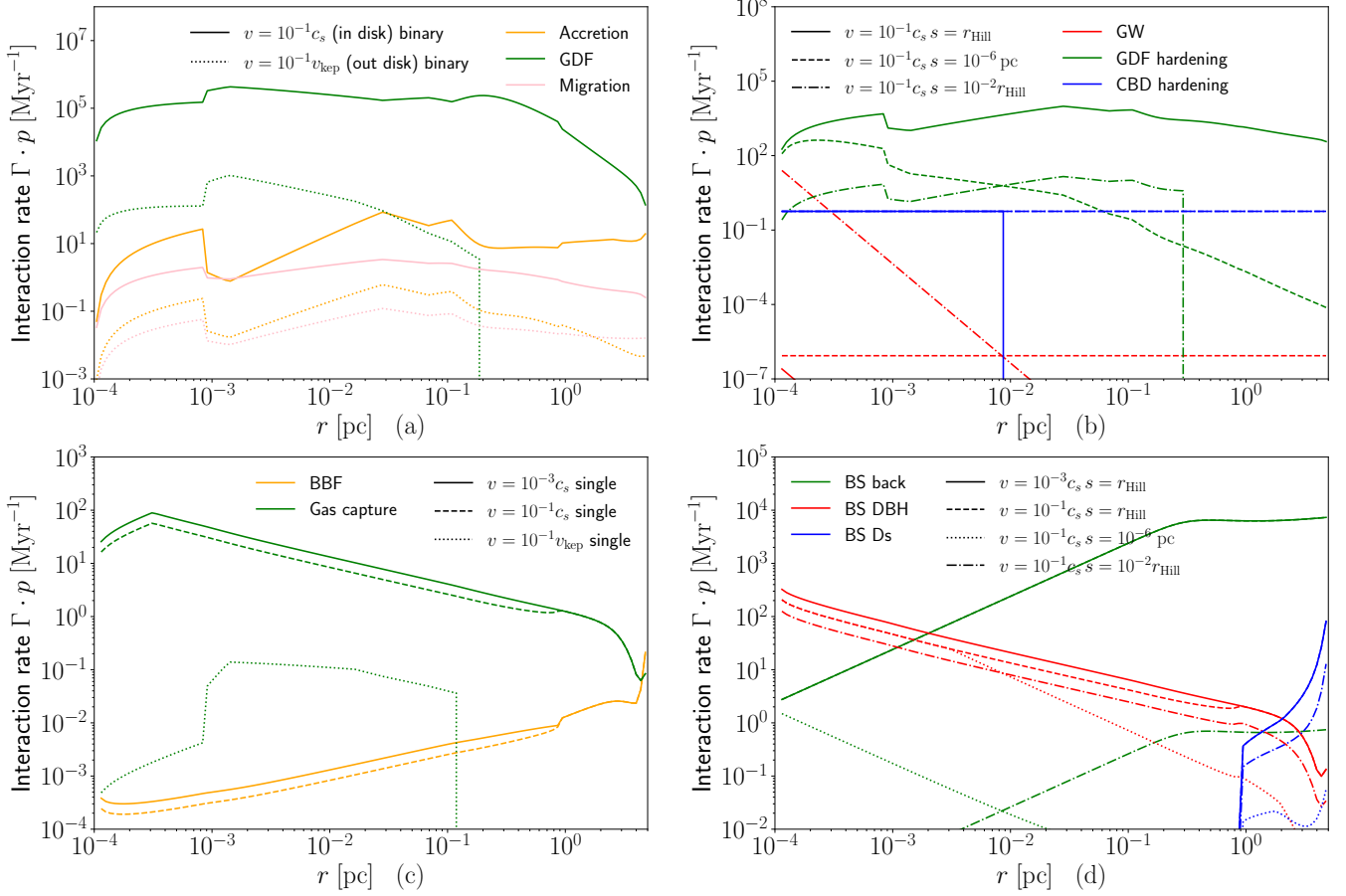


Figure 8. Interaction rate (in Myr^{-1}) of a $10M_{\odot} + 10M_{\odot}$ binary BH and single BH $10M_{\odot}$ using the fiducial model with default SMBH mass ($4 \times 10^6 M_{\odot}$) and Gaussian ($\beta_V = 0.2$) inclination distribution. The relative velocity to disk and the separation of the binary BH is labeled in the figure. Panel (a) shows how the accretion, migration and the gas dynamical friction rate of different relative velocity at different radius. Panel (b) shows how the hardening rate of a $10M_{\odot} + 10M_{\odot}$ binary BH changes due to radius and separation. Panel (c) shows how the binary formation interaction rate of a $10M_{\odot}$ single BH changes at different radius. Panel (d) shows how the binary-single interaction rate with different surrounding components of a $10M_{\odot} + 10M_{\odot}$ binary BH changes due to radius and separation.

(inside the disk components), $v_{x,y,z} = 10^{-1}c_s/\sqrt{3}$ (inside the disk but outside the disk components) or $v_{x,y,z} = 10^{-1}v_{\text{kep}}/\sqrt{3}$ (outside the disk), where $c_s = v_{\text{kep}}(h/r)$ represents the local sound speed of the AGN disk. The choice of outer-disk BH velocity indicates the inclination angle $i = 0.058 \text{ rad} = 3.3^\circ$. The binary's separation is taken as the Hill radius $r_{\text{Hill}}(r, M = 20M_{\odot})$, which is the most newly formed binaries' separation, $10^{-2}r_{\text{Hill}}$, and a fixed separation 10^{-6} pc . In Fig. 8, we account for the fraction of time the BHs spend within the AGN disk p_{disk} or within the disk components p_c . Additionally, we set $p_{\text{uni}} = 0.5$ in the shear velocity equation (Eq. 69) to mitigate randomness.

In Figure 8 (a), the interaction rates for a BH in the AGN disk reveal that gas dynamical friction (green) generally dominates over other interactions. The accretion rate (orange) and migration rate (pink) are typically around 1000 times smaller than the gas dynamical friction rate. For BHs located outside the disk (dotted line in Figure 8 (a) and (c)), the interaction rates are lower due to the factor p_{disk} , particu-

larly for binary formation due to gas capture, which is more likely within the disk environment. Notably, gas dynamical friction does not operate effectively at certain velocities due to the feedback condition Eq. 52, leading to a disappearance in the green line at larger radii, observed in both panels (a) and (c).

In Figure 8 (b), we plot the hardening rate for BH binaries within the disk, as gas hardening occurs only in the disk. When a binary forms at a separation of $s \sim r_{\text{Hill}}$, gas dynamical friction plays a dominant role in hardening the system. As the separation decreases quickly to a smaller value $10^{-2}r_{\text{Hill}}$, the effectiveness of dynamical friction diminishes, while interactions with the circum-binary disk become increasingly significant. These two processes continue to shrink the binary orbit until gravitational wave emission eventually takes over, driving a rapid merger. When the BH binary migrates to smaller radii, the Hill radius r_{Hill} decreases, resulting in a stronger gas dynamical friction rate. Consequently, the transition from gas-hardening dominance to gravitational-wave

dominance occurs over a shorter timescale, effectively accelerating the hardening process (e.g. dash-dot line at small radii). This progression aligns well with our previous understanding of binary mergers in AGN disks.

In Figure 8 (c), binaries form at a very high rate within the AGN disk, primarily due to gas capture. The time fraction spent in the disk components, p_c , has only a minor effect on the interaction rate (solid and dashed lines) when the BH is inside the disk. This process provides an abundant supply of binaries within the AGN disk, facilitating the formation of higher-generation BH binaries from remnant single BHs.

During the migration and hardening process, binary-single interactions with disk stars play a crucial role in shaping binary dynamics. As shown in Figure 8 (d), interactions with background spherical stars (green line) regularly soften newly formed binaries ($s \sim r_{\text{Hill}}$) at large radii. However, as the binary separation decreases, the impact of these interactions diminishes significantly. The interaction rate with disk BHs (red line) and disk stars (blue line) remains relatively unaffected by binary separation and the relative velocity v . Within the AGN disk, binaries frequently undergo binary-single interactions with disk BHs, especially at smaller radii. These encounters rapidly harden the binary but can also eject it from the disk, effectively halting gas-driven hardening and slowing its inward migration toward the center.

We can then construct a binary evolution pathway similar to that presented in Figure 5 of Tagawa et al. (2020b). In AGN disks, BH binaries can form at larger radii, migrate inward, while rapidly hardening through gas dynamical friction. As the binary separation decreases, gas dynamical friction becomes less effective, and circum-binary disk interactions take over as the dominant hardening mechanism. At very small separations, gravitational wave emission ultimately governs the final stage of hardening, leading to the binary's merger into a single BH. Binaries at smaller radii typically transition more quickly from the gas dynamical friction hardening phase to the gravitational wave-driven hardening phase. However, during the inward migration, binaries may undergo multiple binary-single interactions with other disk objects, which can further harden the system but eject the binary from the AGN disk. Ejected binaries can often re-enter the disk relatively quickly, resuming their inward migration and continuing to harden through gas interactions. This dynamic interplay of migration, hardening, and interactions shapes the overall evolution and merger likelihood of BH binaries in AGN disks. Our results align well with those of Tagawa et al. (2020b).

3.2. Merger features

In the binary formation channel, Eqs. 94 and 104 introduce a double-counting effect. To correct for this, we assign a weighting factor to each merger, given by the inverse of the

remnant BH's generation $w = 1/\text{gen}$. The classification of BH generations is defined as follows: pre-existing binaries and binaries formed within the AGN disk are designated as the 0th generation. After a merger, their remnant single BHs become 1st generation BHs. Additionally, pre-existing single BHs and those originating from the AGN disk are also classified as 1st generation. When an n th generation BH forms a binary and subsequently merges, the remnant single BH is classified as $(n + 1)$ th generation.

We primarily consider two inclination (velocity) models: an isotropic distribution and an anisotropic Gaussian distribution with $\beta_v = 0.2$. These two models behave very different in the number of BHs embedded in the disk due to the inclination difference, as shown in Fig. 3. Fig. 9 illustrates the radial and time distribution of mergers for both the Gaussian model (top two rows) and the isotropic model (bottom two rows), categorized by binary formation channel or remnant generation. We assume an AGN lifetime of 100 Myr; however, in our model, the AGN lifetime solely determines the simulation duration and does not affect the AGN disk structure or BH distribution properties. Consequently, the characteristics of mergers in a shorter AGN lifetime scenario can also be inferred from the figure. The averaged Merger rate and top 1% merger mass is plotted in Fig. 10.

It is evident that mergers originating from gas-captured binaries dominate the merger events, occurring at rates approximately $O(10)$ times higher than those of pre-existing binary mergers, both with a slight decline over time. This decrease occurs as disk BHs gradually deplete, while mergers from the dynamical formation and star formation channels continue at a steady rate. Overall, the merger rate across all binary types remains roughly constant, aligning well with Fig. 7 in Tagawa et al. (2020b).

At very early time, we observe a rapid rise in the merger rate, which stabilizes around $t \approx 5$ Myr. The rate peaks at $t \approx 50$ Myr and then slightly decreases for the Gaussian model, while remaining approximately constant for the isotropic model. This divergence stems from the difference in initial inclinations: the Gaussian model contains fewer BHs with large initial inclinations. As a result, the averaged merger rate shows only weak dependence on AGN lifetime, as illustrated in the left panel of Fig. 10.

The merger events are clustered at approximately 10^{-3} pc at early time, with their positions being closer to the SMBH in the isotropic model. These regions of frequent mergers generally correspond to disk BH number densities of $n \approx 10^{13} - 10^{14} \text{ pc}^{-3}$. Such high number densities (calculated by Eq. 120) arise from the extremely low scale height of the disk BH component, as discussed in Section 2.6.2. As time progresses, the location of the critical density shifts outward as shown in the number density map, causing the gathered merger positions to increase correspondingly in the density

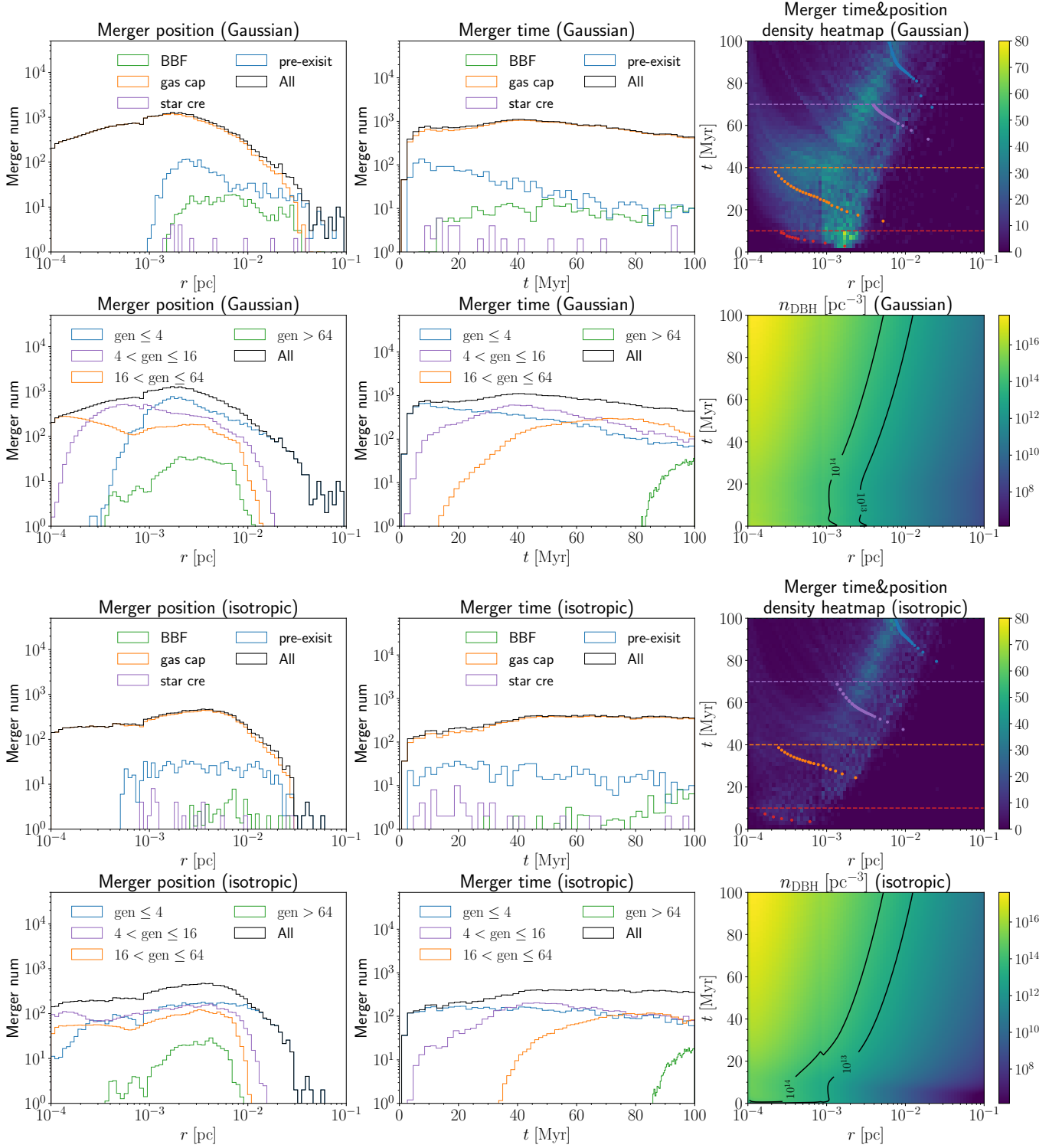


Figure 9. Merger positions and times over 100 Myr (fiducial AGN lifetime: 10 Myr) for the Gaussian model (top two rows) and the isotropic model (bottom two rows). The first column shows the spatial distribution of mergers, while the second column presents the time distribution of mergers, reflecting the shape of the instantaneous merger rate. The black lines represent all mergers, while colored lines distinguish different binary formation types or generations of merger remnants. The third column displays density heatmaps of merger position versus time for the Gaussian model (first row) and isotropic model (third row), with corresponding disk BH number density evolution shown in the second and fourth rows, respectively. The heatmaps also trace the merger history of the most massive merger before 10, 40, 70, and 100 Myr, marked by red, orange, purple, and green dots, respectively. In the number density plots, contours at 10^{13} pc^{-3} and 10^{14} pc^{-3} are overlaid, corresponding well to the bright, high-merger-density regions in the heatmaps.

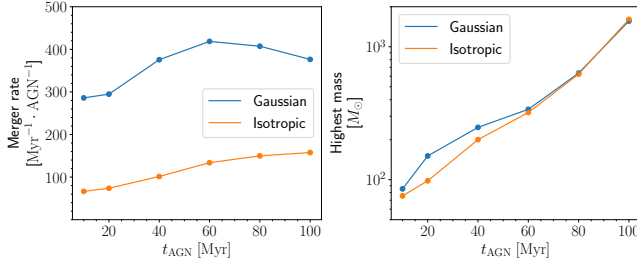


Figure 10. The averaged merger rate and highest 1% merger mass as a function AGN lifetime t_{AGN} . The blue line represent the merger rate for a Gaussian distribution inclination, and the orange line is for an isotropic distribution inclination. The merger rate figure is the averaged merger rate of Fig. 9.

heatmap. A small bump is observed in the merger position figure due to the sudden slow down of migration speed at $r \sim 10^{-3}$ pc (a discontinuous migration trap), which is also visible in the density heatmap of merger time and mass.

Merger remnant generations can reach extremely high values, with a maximum of approximately 100 observed at late times. The highest-generation mergers closely follow their merger time and location, as these BHs require extended time in dense regions of the disk BHs to undergo successive mergers. Mergers of generation greater than 64 are concentrated in the region $10^{-3} - 10^{-2}$ pc, where the high disk BH density facilitates frequent binary-single interactions, providing a continuous supply of binary seeds. Moreover, the high gas density in this region enables BHs to rapidly re-enter the disk, accelerating the hardening and merger process. These very high-generation BHs are typically form at late times ($t \gtrsim 80$ Myr), with their merger masses growing significantly through repeated mergers.

The maximum merger mass increases exponentially with AGN lifetime, as shown in the right panel of Fig. 10. In the density heatmap, we trace the merger history of the most massive mergers before 10, 40, 70, and 100 Myr. The migration speeds of these BHs progressively slow down due to increasing disk BH number densities over time. At $t \lesssim 40$ Myr, the maximum masses in the Gaussian and isotropic models differ slightly, but they converge at long AGN lifetimes, primarily due to the early-time differences in BH number density.

3.3. Merger rate and highest mass

We then estimate the average merger rate during the AGN disk lifetime (in $\text{Myr}^{-1} \cdot \text{AGN}^{-1}$) and average mass of the top 1% merger mass ($M_{\text{BH}} = M_1 + M_2$ in M_{\odot}) according to their merger generations across different parameter configurations listed in Table 1. The average merger rate is given by:

$$\Gamma_{\text{merger}} = \frac{1}{t_{\text{AGN}}} \sum \frac{1}{\text{gen}}, \quad (133)$$

while the average mass of the top 1% of mergers is computed as:

$$M_{\text{top}} = \left(\sum \frac{M_{\text{BH}}}{\text{gen}} \right) / \left(\sum \frac{1}{\text{gen}} \right) \text{ until } \sum \frac{1}{\text{gen}} \geq 1\%. \quad (134)$$

Here, the summation \sum is performed in descending order of BH merger mass. We plot the merger rate and highest mass varied with the parameter (Table 1) in Fig. 11 and Fig. 12.

To assess the impact of various parameters, we define the parametric relevance R as:

$$R = \left(\frac{A_{\text{max}} - A_{\text{min}}}{A_{\text{max}} + A_{\text{min}}} \right) / \left(\frac{f_{\text{max}} - f_{\text{min}}}{f_{\text{max}} + f_{\text{min}}} \right), \quad (135)$$

where A is the merger rate Γ_{merger} or highest mass M_{top} , and f denotes the parameters varied in the simulation. A parameter is considered significant if $R \gtrsim 1$ (colored in red in Table 2), while irrelevant parameters typically correspond to cases where $R \sim \mathcal{O}(0.1)$. Parameters with moderate relevance $R \approx 0.5$, are colored in blue in Table 2. The role of AGN life time is discussed in Sec 3.2, with the trends plotted in Fig 10.

3.3.1. Impact of gas interaction

The gas interaction factors considered are f_{mig} , Γ_{Edd} , $\ln \Lambda_{\text{gas}}$, and the circum-binary disk viscous parameter α_{CBD} , representing the interaction strength of migration, maximum accretion, gas dynamical friction (both for velocity and gas hardening), and gas hardening due to circum-binary disks. Only the migration factor f_{mig} is significant affecting the merger rate and on the merger mass.

Faster migration speeds (larger f_{mig}) mean that BHs spend less time in low gas density regions, thereby accelerating their mergers. Additionally, BHs concentrated in high-density gas regions experience more frequent binary-single interactions, which enhance binary hardening but can also reduce migration speed by ejecting BHs. As illustrated in the upper 2 lines of Fig. 13, the merger time decreases and the merger position gets closer to the center as the migration speeds up.

Interestingly, f_{mig} appears to have little effect on the highest merger mass in the isotropic distribution. While increasing migration speed slightly increases the maximum merger mass in the Gaussian model, the isotropic model reduces the maximum mass slightly. As seen in Fig. 13, high-generation mergers of isotropic model occur at smaller radii, very close to r_{in} , and exhibit little dependence on f_{mig} when $f_{\text{mig}} > 2$. Additionally, in the Gaussian model, no BHs are observed migrating into $r < r_{\text{in}}$ region, whereas in the isotropic model, the BHs migrating into $r < r_{\text{in}}$ increases as f_{mig} increases. This difference arises due to the larger disk BH number density in the Gaussian model, leading to more frequent binary single interactions and the increased potential for higher-generation mergers. Notably, under realistic

Parameter relevance R					
Type	Symbol	Merger rate (Gaussian)	Highest mass (Gaussian)	Merger rate (Isotropic)	Highest mass (Isotropic)
SMBH	$\log_{10}(M_{\text{SMBH}}/M_{\odot})$	3.271664742	2.283997134	3.227080137	1.481548969
AGN disk	$r_{\text{disk,out}}$	0.150934513	0.479450428	0.325568885	0.254059658
AGN disk	$r_{\text{disk,in}}$	0.367946993	0.470898416	0.227961833	0.048850026
AGN disk	$\dot{M}_{\text{out}}/(0.1\dot{M}_{\text{Edd}})$	0.128298205	0.149516024	0.123283759	0.01802458
AGN disk	m_{AM}	0.975586098	0.568123545	0.869958957	0.213075973
AGN disk	α_{SS}	0.26617256	0.291467832	0.29347429	0.234098288
AGN disk	ϵ	0.476165094	0.214333161	0.148482635	0.048634006
AGN disk	t_{AGN}	0.241828557	1.094862877	0.51226985	1.115050771
AGN disk	β_{cre}	0.079517332	0.113970213	0.315327243	0.060308176
Mass distribution	β_{IMF}	0.085197411	0.222676003	0.219689462	0.209508684
Mass distribution	$M_{\text{BH,ini,max}}$	0.051343959	0.199015371	0.150541924	0.609525054
Radial distribution	$1 + \gamma_{\rho}$	0.71035059	0.174521094	1.519590275	0.440812756
Radial distribution	$N_{\text{BH,ini}}$	0.995658439	0.273836794	1.043597729	0.168824286
Radial distribution	$r_{\text{BH,out}}$	0.911899634	0.20054724	1.16909195	0.143582742
Velocity distribution	β_v	1.201186702	0.086831942	NA	NA
Binary	f_{pre}	0.076102625	0.023543428	0.114463463	0.132984591
Binary	R_{max}	0.064121306	0.069069019	0.071751937	0.026716585
Gas interaction	f_{mig}	0.966145685	0.463338762	1.06062715	0.17690834
Gas interaction	$\ln \Lambda_{\text{gas}}$	0.047618704	0.08551462	0.179980313	0.080284549
Gas interaction	$0.1\Gamma_{\text{Edd}}/\eta_c$	0.147286371	0.159534718	0.055696851	0.113834999
Gas interaction	α_{CBD}	0.016120167	0.023155906	0.030935634	0.006721593

Table 2. The parametric relevance R (defined in Eq. 135) for pre-existing BHs (including the star forming “pre-existing” binaries) during the simulation under isotropic and Gaussian distributions of inclination. The plot range of each parameter is listed in Table 1. The red cells represent the parameter plays an important role ($R > 0.75$) and the blue cells means this parameter is relevant but less important ($0.4 < R < 0.75$) to the merger rate / highest mass for Gaussian / isotropic distribution. We estimate the relevance of $(1 + \gamma_{\rho})$ instead of γ_{ρ} to remove the singularity in Eq. 135.

conditions, f_{mig} varies with radial distance on a small scale but remains around $f_{\text{mig}} \sim 2.0$, as discussed in Sec. 4.3.

The maximum accretion rate Γ_{Edd} which typically increases BH masses, has a low relevance $R \sim 0.2$ for the merger mass, making it nearly insignificant. In Figure 15 of Tagawa et al. (2020b), the accreted mass of BH binaries during mergers is generally $O(0.1)$ of their initial mass, and our results align with this conclusion.

The gas dynamical friction factor $\ln \Lambda_{\text{gas}}$, which affects the rate of BHs migrating into the disk and the scale height of disk components on an $O(1)$ scale, is largely irrelevant. Its impact is limited to scenarios where BHs are near/in the AGN disk, and it diminishes logarithmically outside the AGN disk, as shown in Figure 5.

The circum-binary disk viscous parameter α_{CBD} is of minor importance, with $R_{\text{CBD}} \sim O(0.1)R_{\text{GDF}}$, indicating that gas hardening due to the circum-binary disk is a secondary effect compared to gas dynamical friction hardening. This conclusion is supported by hydrodynamical simulations (Baruteau et al. 2010; Li et al. 2022; Rowan et al. 2023).

3.3.2. Impact of BH populations

The BH mass parameters naturally play a significant role in determining merger masses. As expected, increasing the maximum mass of pre-existing single BHs leads to a higher upper limit on merger mass, while the overall merger rate remains relatively unchanged. However, we observe that the initial mass function index β_{IMF} and the initial maximum single mass $M_{\text{BH,ini,max}}$ exhibit little relevance to either the merger rate or the highest merger mass, except for the highest mass of the isotropic distribution. This suggests that increases in individual BH masses are diluted by frequent binary-single interactions and binary formation, which promote hierarchical mergers across multiple generations. In contrast, the isotropic distribution, which has fewer disk BHs, relies more heavily on the initial single BH mass to determine the highest merger mass.

Parameters related to the spatial distribution significantly affect the merger rate but have minimal impact on merger masses. These parameters, γ_{ρ} , $N_{\text{BH,ini}}$ and $r_{\text{BH,out}}$ determine the BH number density near the SMBH (Eq. 8), influenc-

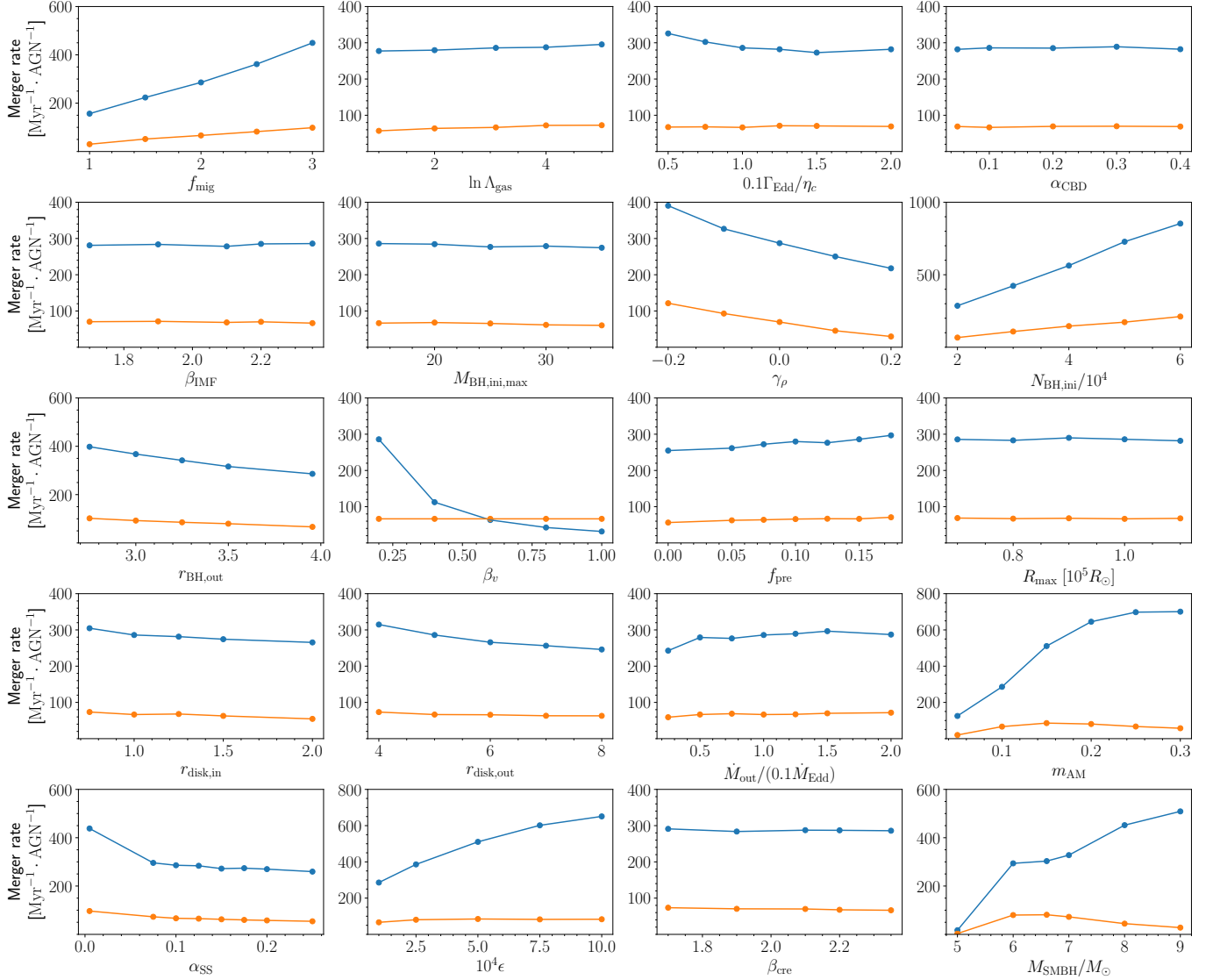


Figure 11. The averaged merger rate as a function of different parameters listed in Table 1 (except for t_{AGN}). The blue line represent the merger rate for a Gaussian distribution inclination, and the orange line is for an isotropic distribution inclination.

ing the merger rate without substantially altering the highest merger mass. The inclination distribution, particularly β_v in the Gaussian model, governs the number of BHs that settle into the disk, serving as potential seeds for binary formation and binary-single interactions. All these parameters are at least relevant to the merger rate, and changing γ_ρ becomes a more effective way to increase the number density of disk BHs for isotropic model.

The pre-existing binary fraction f_{pre} and the initial maximum separation R_{max} both have negligible influence on both the merger rate and the highest BH mass. These two parameters mainly determine the gen=1 BH remnants, which is a secondary effect compared to the higher generation binaries both to merger rate and highest mass. What's more, the separation rapidly decreases due to gas dynamical friction

hardening as BHs migrate into the disk, making the initial separation less important.

3.3.3. Impact of disk parameters

In our analysis of disk parameter effects, we examine the influence of the AGN disk size ($r_{\text{disk,in}}$, $r_{\text{disk,out}}$), accretion rate at the outer disk boundary \dot{M}_{out} , the angular momentum transport rate m_{AM} , Shakura-Sunyaev α -parameter α_{SS} , the conversion efficiency ϵ , and the star-formation initial mass function index β_{cre} . Some disk variables, like m_{AM} , are analyzed beyond their typical range (m_{AM} is normally 0.1-0.2) to assess their influence. The AGN lifetime t_{AGN} is unique in that it only extends the simulation duration, thereby increasing the maximum merger mass without affecting the merger rate a lot, as discussed in Sec. 3.2.

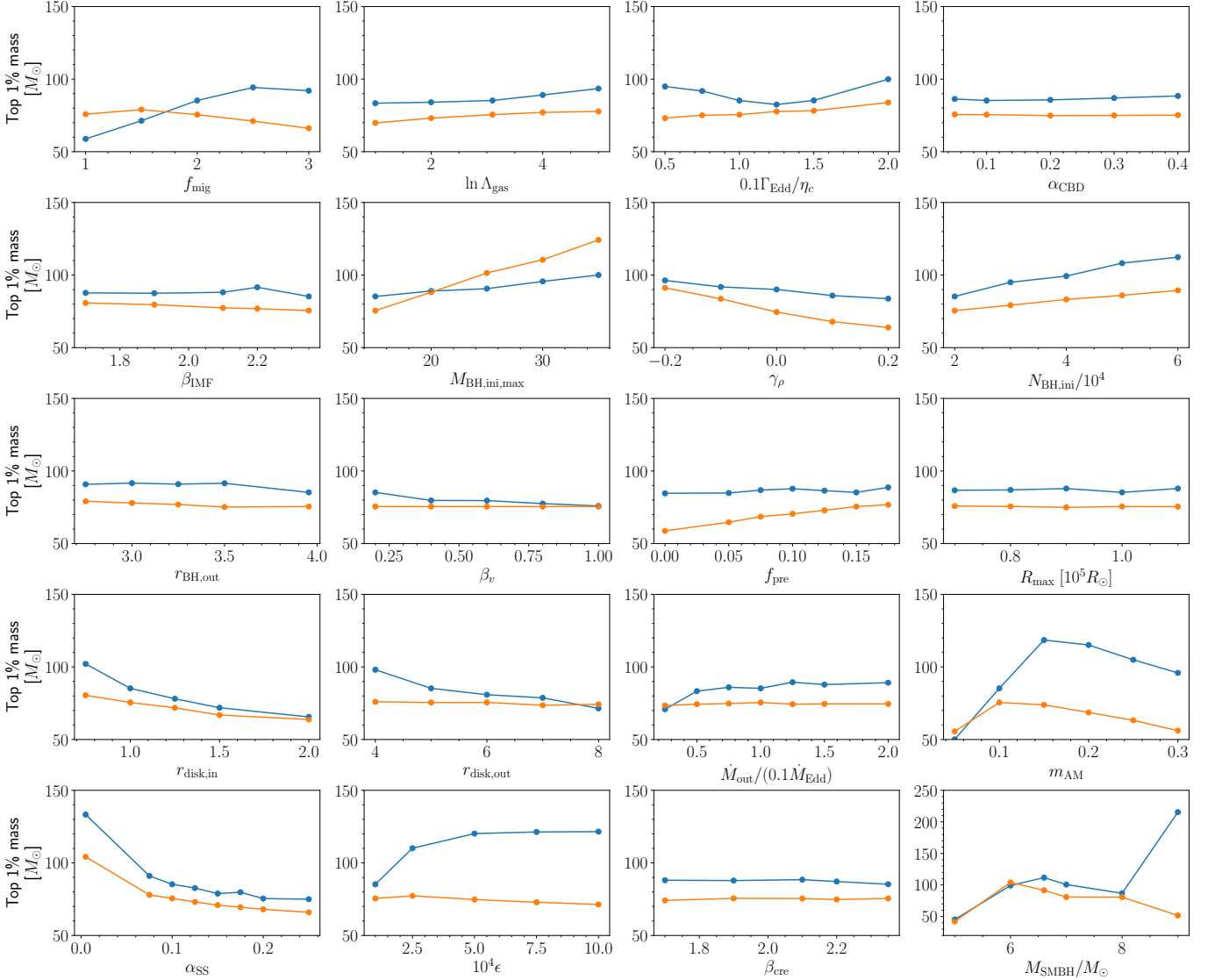


Figure 12. Highest 1% merger mass as a function of different parameters listed in Table 1 (except for t_{AGN}). The blue line represent the merger rate for a Gaussian distribution inclination, and the orange line is for an isotropic distribution inclination.

Among these disk parameters, the angular momentum transport rate m_{AM} has a significant impact on the merger rate in both the isotropic and Gaussian distributions, whereas the conversion efficiency ϵ plays a comparatively minor role, primarily affecting the merger rate of Gaussian distribution. Regarding the maximum merger mass, parameters such as the inner and outer AGN disk radii ($r_{\text{disk,in}}$, $r_{\text{disk,out}}$), and m_{AM} primarily influence the Gaussian distribution, while their effect on the isotropic distribution remains relatively small.

While all disk parameters influence disk properties, minor variations in these parameters may result in negligible changes in scale height or gas density. However, certain variations can significantly impact the merger rate, primarily due to their effect on type I/II migration of BHs within the disk. Changes in disk properties can lead to variations in migration speed by a factor of ~ 2 , thereby influencing the merger rate.

Notably, parameters such as m_{AM} and ϵ induce by a factor of ~ 2 changes in migration speed at $r \sim 10^{-4} - 10^{-1}$ pc. In contrast, the Shakura-Sunyaev viscosity parameter (α_{SS}) affects migration speed only at $r \lesssim 10^{-3}$ even when varied to an extremely small value $\alpha_{\text{SS}} = 0.005$, resulting in minimal impact on the merger rate, as illustrated in Fig. 13 and 14.

Modifying both the inner and outer sizes of the AGN disk significantly affects the maximum merger mass in the Gaussian distribution but generally has a minor impact on the isotropic distribution. With a migration speed variation of at most a factor of < 2 , we observe a noticeable decrease in the number of high-generation mergers when increasing either $r_{\text{disk,out}}$ or $r_{\text{disk,in}}$. This decline may be attributed to the substantial difference in number density at $r \sim 2 \times 10^{-4}$ pc. However, this effect is prominent only in the Gaussian distribution, as the number of disk BHs in the isotropic model

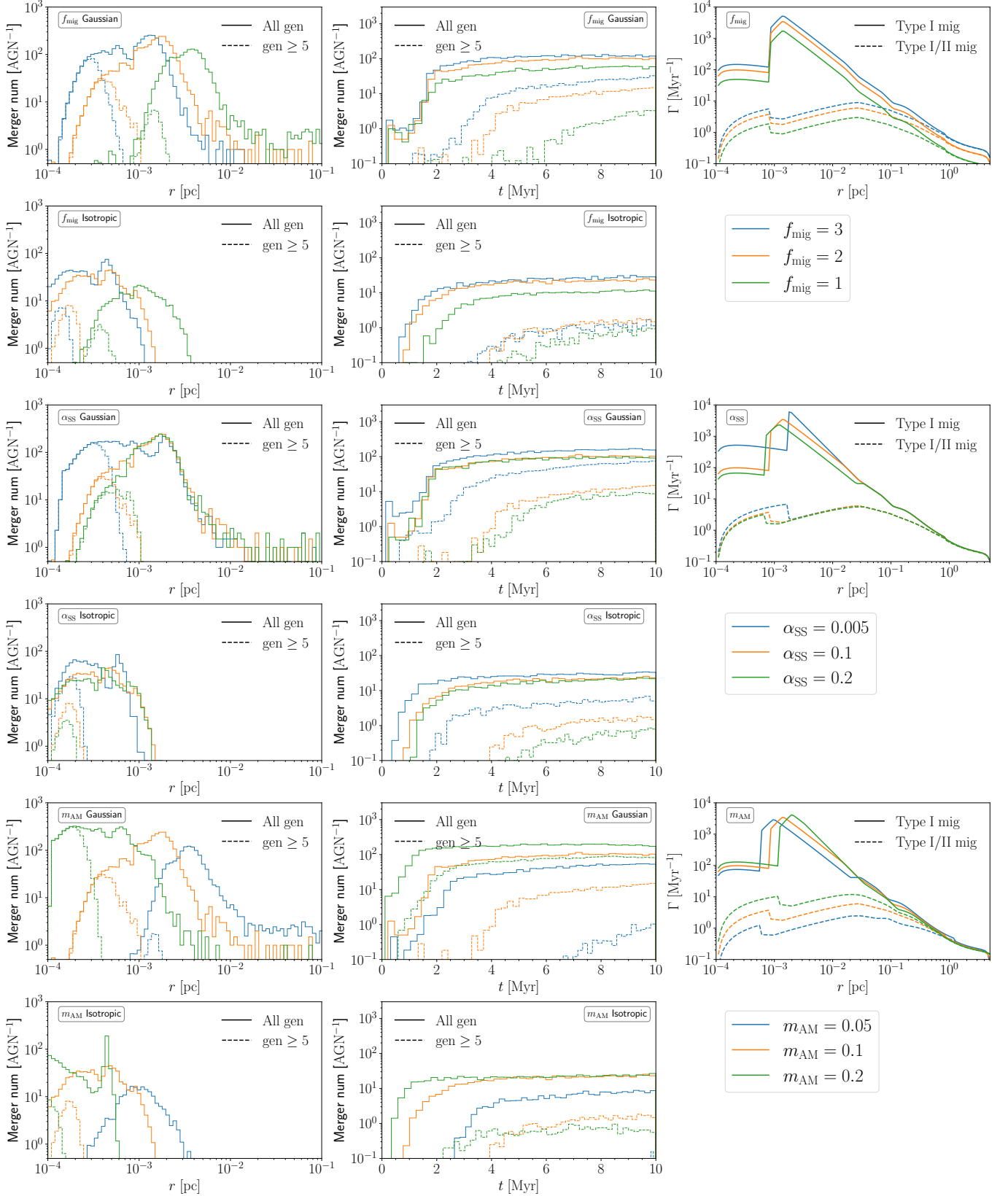


Figure 13. Correlation between merger time, position, and migration rate for isotropic and Gaussian distributions due to different parameter variations. The plotted merger radii range from $10^{-4} \sim 10^{-1}$ pc, covering the region where most mergers occur. The dashed line represents the distribution of remnants with generation ≥ 5 where most high-mass mergers are found. The three rightmost panels show the migration rate for a $10M_{\odot}$ BH comparing Type I migration (solid line) and Type I/II migration (dashed line). This plot includes variations in the migration factor f_{mig} , vicious α parameter α_{SS} , and angular momentum transport rate m_{AM} .

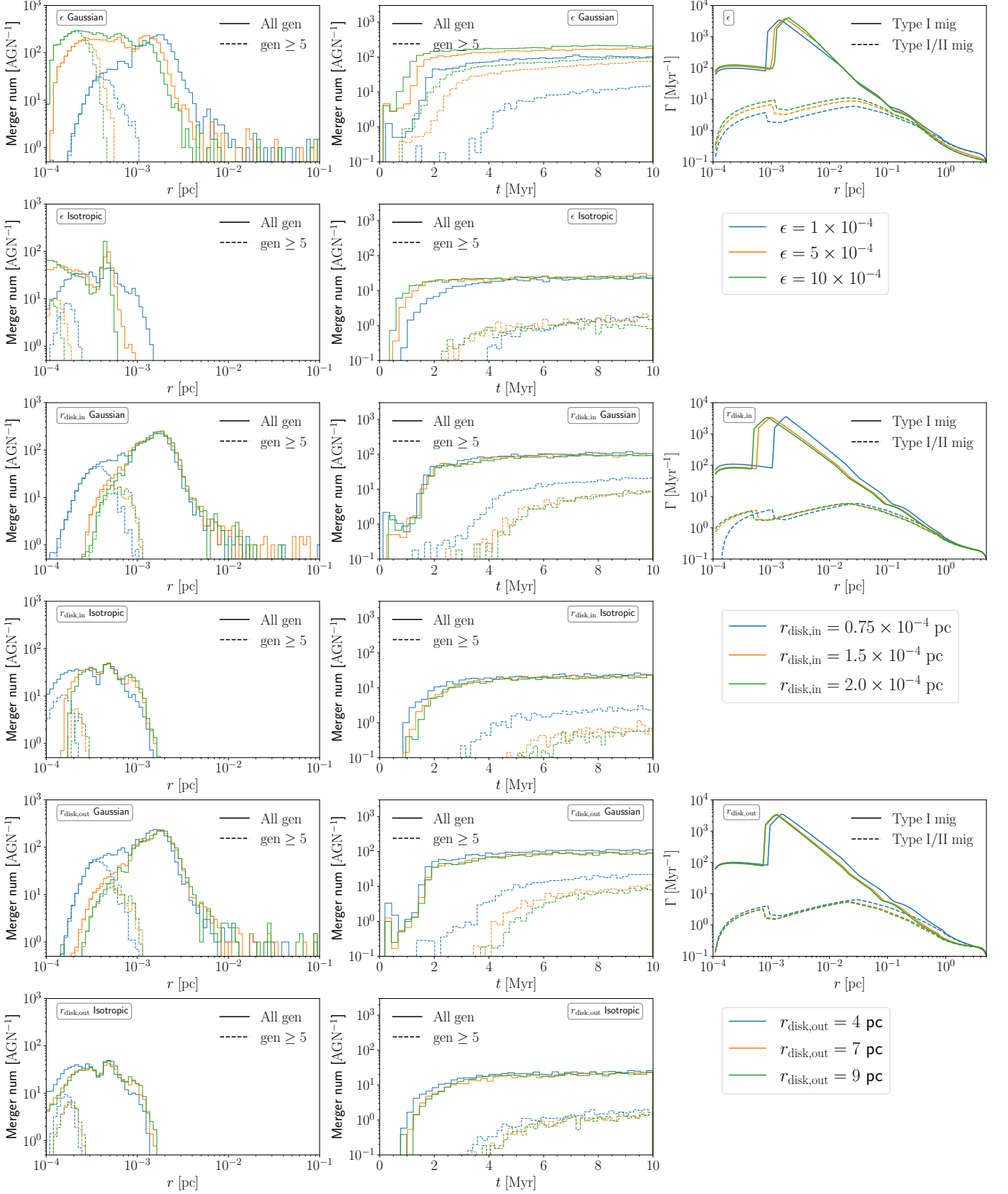


Figure 14. Same as Fig. 13. This plot includes variations in the conversion efficiency ϵ , AGN disk inner size $r_{\text{disk,in}}$, and AGN disk outer size $r_{\text{disk,out}}$.

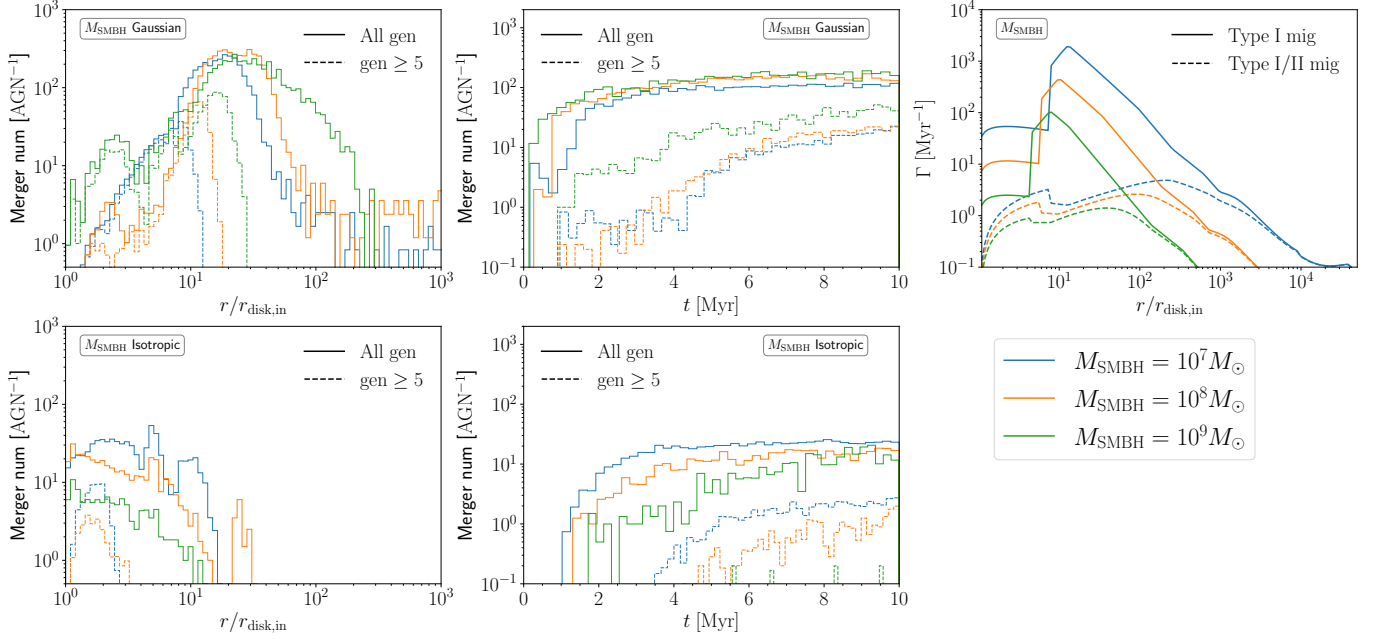


Figure 15. Same as Fig. 13. This plot includes variations in the SMBH mass $M_{\text{SMBH}} = 10^7 - 10^9 M_{\odot}$. The radius is rescaled to $r/r_{\text{disk,in}}$.

is insufficient to reveal a similar trend. Notably, when α_{SS} takes very small values, it induces a similar trend in the maximum merger mass, it induces a similar trend in the maximum merger mass, but its effect is not significant enough to be considered a relevant parameter.

Surprisingly, direct changes to the accretion rate at outer radius \dot{M}_{out} have a less pronounced effect on the merger rate compared to variations in m_{AM} and ϵ . While increasing \dot{M}_{out} generally enhances the star formation rate, leading to minimal influence on the inner regions of the AGN disk. As a result, as long as \dot{M}_{out} varies within its typical range, both the number density and migration speed remain largely unchanged, making its impact relatively insignificant. However, significant changes in $r_{\text{disk,out}}$ could, in turn, influence the accretion rate at $r_{\text{out}} = 5$ pc, potentially altering the merger dynamics affecting the merger rate and mass.

3.3.4. Impact of SMBH mass

Changes in SMBH mass can lead to complex effects on both the merger rate and the maximum merger mass. As shown in Fig. 13 and Fig. 14, when the SMBH mass is below $10^7 M_{\odot}$, the merger rate and maximum BH mass remain very low, primarily constrained by the initial number of BHs in the disk. As the SMBH mass increases, both the merger rate and maximum mass stabilize around $10^6 - 10^7 M_{\odot}$.

However, for $M_{\text{SMBH}} \gtrsim 10^7 M_{\odot}$, the merger rate and maximum mass exhibit divergent trends between the isotropic and Gaussian distributions. In the isotropic distribution, fewer mergers and hierarchical mergers occur due to the limited number of disk BHs, as shown in Fig. 15. In contrast, for the Gaussian distribution, the merger rate increases significantly,

while higher-generation mergers occur at smaller radii, leading to a substantial increase in the maximum merger mass.

We can roughly estimate the two major factors influence the merger rate and mass. First, the type I/II migration speed at small radii remains roughly constant at the same normalized radius, $r_0 = r/r_{\text{disk,in}}$, regardless of SMBH mass (Fig. 6). However, at larger radii, the migration speed slows down as SMBH mass increases. This should reduce the merger rate while it takes more time to migrate to dense gas region.

Second, we estimate the disk BH number density at the same r_0 as:

$$n(r_0) \propto \frac{N_{\text{BH,ini}}}{r_0^2 r_{\text{disk,in}}^3 h_{\text{DBH}}(r_0)} \propto \frac{M_{\text{SMBH}}}{r_0^3 r_{\text{disk,in}}^3} \frac{v_{\text{kep}}}{\sigma_{\text{DBH}}} \propto M_{\text{SMBH}}^{-1/4}, \quad (136)$$

where we use the velocity dispersion estimate from Eq. 127, gas dynamical friction interactions from Eq. 51, the sound speed relation $c_s = v_{\text{kep}}(h/r)$, and the disk size from Eq. 29. This suggests that a higher SMBH mass leads to a slightly lower disk BH number density, reducing the binary-single interaction rate and binary formation rate, ultimately decreasing the overall merger rate. This effect becomes significant when the disk BH population is insufficient for frequent hierarchical mergers, as seen in the isotropic distribution. However, for the Gaussian distribution, even with a factor of $10^{-1/4} \approx 1/3$ decrease in number density compared to fiducial mass, the number of BHs remains sufficient to sustain enough hierarchical mergers.

A key factor explaining the trend difference is the critical number density for hierarchical mergers discussed in Sec. 3.2. In the Gaussian distribution, this density thresh-

old persists at early times but shifts closer to the SMBH as M_{SMBH} increases, facilitating more hierarchical mergers and leading to a higher maximum merger mass. In contrast, for the isotropic distribution, this critical number density fails to emerge, particularly in environments with a high SMBH mass, making it difficult to sustain high-generation mergers.

3.3.5. Implications

Combining the results from Sec. 3.2 with our previous discussion, we identify several key factors influencing both the merger rate and the highest merger mass. If a disk parameter modifies the Type I/II migration rate on the order of $O(1)$, it typically affects the merger mass by facilitating the migration of binaries into high-density gas regions, thereby enhancing binary hardening. Additionally, if a disk parameter variation moves the location of a migration trap (due to discontinuities in disk properties) at $O(1)$ scale, it can slow down inward migration at small radii, increasing the likelihood of hierarchical mergers and contributing to a higher maximum merger mass.

Parameters that directly increase the number of disk BHs also tend to raise the merger rate, as binary-single interactions play a crucial role in the binary hardening process. If the increase in disk BH numbers is substantial, it can further elevate the maximum merger mass, similar to the effect of modifying a migration trap. This effect is particularly pronounced in the isotropic model, where the number of disk BHs is initially insufficient to sustain frequent binary-single interactions and binary formations.

A sufficiently long AGN lifetime would smooth out the structure of merger positions and times, as the merger rate and the rate of BHs migrate into $r < r_{\text{in}}$ both approach a steady-state value. While migration speed remains a key factor influencing the merger rate, its impact on the maximum merger mass diminishes over time. This is evidenced by the fact that f_{mig} becomes irrelevant to the highest merger mass of isotropic distribution.

4. DISCUSSION

4.1. Convergence Test

We examined the impact of numerical resolution on the merger rate and the highest merger mass by varying the number of radial cells (N_{cell}), the number of mass cell (N_{mass}) and the time step parameter η_t . When adjusting the number of radial cells to $N_{\text{cell}} = 80, 160$, the merger rate Γ_{merger} changed by only $\sim 2\%$ for both Gaussian model, while the top 1% mass M_{top} changes 15% and 8% for Gaussian model. In contrast, for the isotropic model, both the merger rate and top 1% mass both changed by less than 4%. The slower convergence of the Gaussian model likely stems from its higher merger rate, where 10,000 mergers may not be sufficient for full statistical convergence.

When varying the number of mass cells to $N_{\text{mass}} = 80, 120$, the merger rate Γ_{merger} and the top 1% mass M_{top} exhibited only minor fluctuations of 1%-5% for both isotropic and Gaussian model. Additionally, we tested the time step parameter at $\eta_t = 0.05$ and $\eta_t = 0.2$. For both Gaussian and isotropic model, the merger rate and highest mass changes by $\sim 15\%$ for $\eta_t = 0.05$ and $\eta_t = 0.2$. However, with the $\eta_t = 0.05$ applied, the time cost becomes incredibly large (increase by more than 5 times from $\eta_t = 0.1$). This larger variation arises because the weak scattering diffusion term scales as $\sqrt{\Delta t}$, as indicated in Eq. 75. Although convergence is slower for the Gaussian distribution, our main conclusions regarding the trends of parameter variations remain unaffected by numerical resolution. In the next section, we provide potential methods to solve this issue.

4.2. Limitations

In our program, we adopt a highly simplified model at the statistical background level. We assume a collisionless BH disk with scale height h_{DBH} , neglecting both binary-single interactions and binary formation processes. While this approximation may hold in non-collisional or weakly collisional systems, it introduces several limitations and potential inaccuracies in the context of AGN disks, where dynamical interactions are expected to be significant.

First, the collisionless assumption breaks down in the inner regions of the disk, where the binary-single interaction rate becomes comparable to the gas interaction rate (as shown in Fig. 8). These interactions play a crucial role in slowing BH migration and enriching the BH population. Neglecting them leads to an underestimated migration timescale in these regions. Moreover, binary-single interactions can eject BHs from the disk, temporarily reducing the local number density. Although ejected BHs may return to the disk on low-inclination orbits, this recycling process introduces a time delay in the buildup of the BH population. This effect is likely less significant in AGNs with shorter lifetimes, where such interactions are confined to smaller radii, and in isotropic models, where the overall number density of disk BHs is relatively low.

Second, neglecting interactions leads to an overestimation of the local BH number density and thus an inflated binary formation rate. Although we apply a correction at the Monte Carlo stage using Eq. 70 to account for number reduction due to binary formation, this only considers binaries formed within the simulated BH sample. Background BHs that are not explicitly tracked can also form binaries and deplete the local population—an effect not included in our current model. As a result, the background BH number density remains systematically overestimated.

Third, by ignoring binary formation in the background, we implicitly assume that all binary partners are drawn from the

first-generation BH population. In other words, only 1g+Ng hierarchical mergers are included, while Mg+Ng mergers involving two higher-generation BHs are omitted. This constraint affects the merger weighting in Eqs. 133 and 134, leading to an overestimated merger rate and potentially underestimating the maximum BH mass attainable in the system.

A potential solution to address all three issues is to explicitly track single and binary BH populations at the background level, while incorporating higher-generation mergers. However, this requires accurately modeling binary-single interactions, including ejection and re-entry processes, without significantly increasing computational cost—a challenge we aim to tackle in future work.

Finally, the artificially high BH number density may have additional consequences. At late times, the total BH mass could approach or even exceed the local AGN disk mass, leading to significant dynamical feedback on the disk itself. These concerns are model-dependent, but they highlight the importance of developing a more realistic treatment of BH dynamics in AGN disks.

4.3. Migration Traps and Extreme Mass-ratio Inspirals

As discussed in Section 2.4.3, a BH orbiting within a gas disk exchanges angular momentum with its surroundings, leading to net inward radial migration. [Paardekooper & Mellema \(2006\)](#) demonstrated that, under certain conditions, migration can proceed outward, resulting in the formation of a migration trap where outwardly migrating objects meet inwardly migrating ones. Such migration traps have been predicted in protoplanetary disks ([Lyra et al. 2010](#)) and in AGN disks, as suggested by [Bellovary et al. \(2016\)](#) using the torque formula from [Paardekooper et al. \(2010\)](#). Numerous studies highlight their significance in contributing to hierarchical mergers ([McKernan et al. 2012](#); [Yang et al. 2019](#); [Tagawa et al. 2020b](#); [Santini et al. 2023](#); [Gilbaum & Stone 2022](#); [Vaccaro et al. 2024](#)).

However, recent studies have challenged the existence of migration traps in AGN disks. [Peng & Chen \(2021\)](#) found that the outward migration region vanishes when considering the torque exerted by mini-disks surrounding black holes due to gas drag. [Pan & Yang \(2021\)](#) reached a similar conclusion, accounting for the influence of density wave generation and headwind effects. [Grishin et al. \(2024\)](#), employing an updated torque formula from [Jiménez & Masset \(2017\)](#), also observed the disappearance of the outward migration region. However, [Grishin et al. \(2024\)](#) introduced the role of thermal torque, generated by the thermal response of the AGN to black holes accreting via their own mini-disks, which in turn facilitates the formation of migration traps. [Gangardt et al. \(2024\)](#) then applied this mechanism to the AGN disk model

from [Thompson et al. \(2005\)](#) and [Sirko & Goodman \(2003\)](#), successfully recovering migration traps at various radii.

The aforementioned studies consider only Type I migration torque, which is the direct summation of corotation torque and Lindblad torque. In AGN disks, the gap-opening condition is typically satisfied when $K \gtrsim 20$ ([Kanagawa et al. 2018](#)), where K is defined in Eq. 38. Given that our disk model is very thin $h/r \sim 10^{-3}$, this condition is easily met at small radii. We thus normalize the type I and type I/II migration interaction rates as $\Gamma_I = C_I \Gamma_0$ and $\Gamma_{I/II} = C_{I/II} \Gamma_0 / (1 + 0.04K)$, where

$$\Gamma_0 = 2 \left(\frac{M_{\text{BH}}}{M_{\text{SMBH}}} \right) \left(\frac{2\rho r^2 v_{\text{kep}}}{M_{\text{SMBH}}} \right) \left(\frac{h}{r} \right)^{-1}, \quad (137)$$

and adopt the formulation from [Kanagawa et al. \(2018\)](#) to account the gap opening:

$$C_{I/II} = C_L + C_C \exp(-K/K_t), \quad K_t = 20. \quad (138)$$

Here, the subscripts L and C represent the Lindblad and corotation torques, respectively, with the latter often simplified to a horseshoe drag in the nonlinear regime. We explore the coefficients derived in [Paardekooper et al. \(2010\)](#) (*p10*) and [Jiménez & Masset \(2017\)](#) (*jim17*):

$$C_L = \begin{cases} -2.5 + 0.1\nabla_\Sigma + 0.5\nabla_T & p10_iso \\ (-2.5 + 0.1\nabla_\Sigma - 1.7\nabla_T)/\gamma_{\text{gas}} & p10_ad \\ -2.34 + 0.1\nabla_\Sigma - 1.5\nabla_T & jim17_iso \\ (-2.34 + 0.1\nabla_\Sigma - 1.5\nabla_T) f_\gamma \left(\frac{\chi}{\chi_c} \right) & jim17_tot \end{cases} \quad (139)$$

and

$$C_C = \begin{cases} 1.65 - 1.1\nabla_\Sigma - 1.4\nabla_T & p10_iso \\ (1.65 - 1.1\nabla_\Sigma + 7.9\nabla_S/\gamma_{\text{gas}})/\gamma_{\text{gas}} & p10_ad \\ 0.976 - 0.64\nabla_\Sigma + \nabla_T & jim17_iso \\ (0.46 - 0.96\nabla_\Sigma + 1.8\nabla_T)/\gamma_{\text{gas}} & jim17_tot \end{cases} \quad (140)$$

where $\nabla_\Sigma = -d \ln \Sigma / d \ln r$, $\nabla_T = -d \ln T / d \ln r$, and the entropy gradient can be written as $\nabla_S = -d \ln S / d \ln r = \nabla_T - (\gamma_{\text{gas}} - 1)\nabla_\Sigma$. We adopt $\gamma_{\text{gas}} = 5/3$ as the fiducial adiabatic index. The function $f_\gamma(\chi/\chi_c)$ is defined as $f_\gamma(x) = (\sqrt{x/2} + 1/\gamma_{\text{gas}})/(\sqrt{x/2} + 1)$, with

$$\chi = \frac{16\gamma_{\text{gas}}(\gamma_{\text{gas}} - 1)\sigma_{\text{SB}}T^4}{3\rho^2 c_s^2 \kappa}, \quad \chi_c = \frac{c_s^2}{\Omega} \quad (141)$$

The [Bellovary et al. \(2016\)](#) (*b16*) combines the adiabatic and isothermal torque in [Paardekooper et al. \(2010\)](#) (*p10*), expressed as

$$C_{L,C} = \frac{C_{L,C}^{ad} \Theta^2 + C_{L,C}^{iso}}{(1 + \Theta)^2}, \quad b16 \quad (142)$$

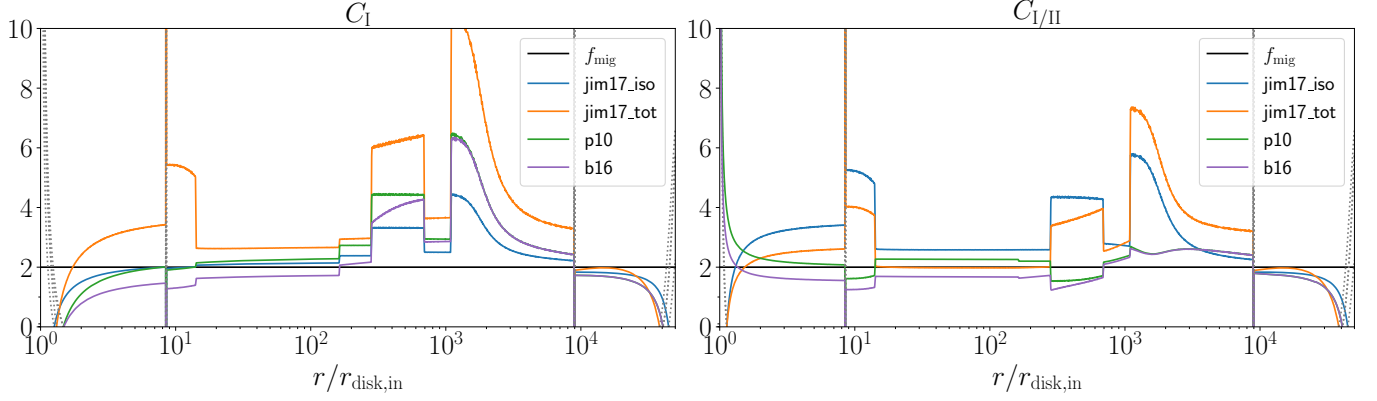


Figure 16. The migration normalized factor C_I and $C_{I/II}$ for type I and type I/II migration. The black line represent our simplified model $f_{\text{mig}} = 2$ using in the simulation. Additionally, we plot torque models from Jiménez & Masset (2017) (*jim17*) for both isothermal (*jim17_iso*, blue) and non-isothermal cases (*jim17_tot*, orange), Paardekooper et al. (2010) (*p10*, green) for the isothermal case, and Bellovary et al. (2016) (*b16*, purple), which adopts the formula from Paardekooper et al. (2010). The gray dotted line indicates regions where the torque results in outward migration.

where the dimensionless factor Θ is the ratio of the radiative and dynamical timescales, defined in Lyra et al. (2010) as:

$$\Theta = \frac{k_B(v_{\text{kep}}/r)\tau_{\text{eff}}}{12\pi m_{\text{gas}}(\gamma_{\text{gas}} - 1)\sigma_{\text{SB}}T^3}, \quad (143)$$

and effective optical depth is given by:

$$\tau_{\text{eff}} = \frac{3\tau}{8} + \frac{\sqrt{3}}{4} + \frac{1}{4\tau}. \quad (144)$$

Fig. 16 illustrates how the migration factors C_I and $C_{I/II}$ for a $10M_{\odot}$ BH vary with radius in our fiducial SMBH and AGN disk model. The gray dotted line marks regions experiencing outward migration torque, while the different colored lines correspond to different torque models. We observe the formation of a narrow migration trap at $r \sim r_{\text{disk,in}}$ and $r \sim 10^4 r_{\text{disk,in}}$, arising from discontinuities in surface density and temperature. Pan & Yang (2021) demonstrated that these migration traps are caused by opacity gaps and can be nullified by incorporating a more accurate radiation pressure equation. In our simulation, we account for this effect by directly adjusting the migration speed at the discontinuity, as depicted in Figure 6. This effectively assumes that all BHs traverse the narrow discontinuity trap while experiencing a slowdown in migration. A potential “pile-up” region may emerge near $r_{\text{disk,in}}$, except when using the Type I/II migration factor from the Bellovary et al. (2016) model. The existence of such a trap region depends on a correction factor $(1 - \sqrt{r_{\text{disk,in}}/r})$ for the accretion rate \dot{M} at inner region. Although this factor generates persistent outward torque, our chosen $r_{\text{disk,in}}$ is typically too large due to model limitations. If a more refined model were applied with $r_{\text{disk,in}} \sim 6R_g = 6GM_{\text{SMBH}}/c^2$, this region might vanish or become dominated by the gravitational radiation from Extreme Mass Ratio Inspirals (EMRIs) (Grishin et al. 2024). While

Grishin et al. (2024) introduced thermal torque as a mechanism to reinstate migration traps, its behavior in gap-opening regions remains unstudied and may not be directly applicable to this AGN disk model. Additionally, an outward migration region may emerge at $r \sim r_{\text{disk,out}}$, potentially preventing stars and BHs formed at very large radii from migrating inward. Since BHs from star formation have a negligible influence on the overall process, this effect can be considered insignificant. However, our results indicate that variations in migration speed can substantially impact both the merger rate and the maximum merger mass. Given this, and in light of Figure 16, a more precise treatment of migration speed is necessary for accurate predictions.

We can estimate the number of EMRI events in our simulation by tracking the number of BHs that migrate into $r < r_{\text{in}}$. However, due to computational constraints, our fiducial AGN lifetime of $t_{\text{AGN}} = 10$ Myr is insufficient to observe such BHs in the Gaussian models. In contrast, for the isotropic models, we find an average of 10.35 BHs with a total mass of $132M_{\odot}$ migrate into this region. This aligns with the reduced binary-single interactions in the isotropic model. Consequently, even if a migration trap forms at $r \sim r_{\text{in}}$, it would only accumulate a total mass of $132M_{\odot}$ within 10 Myr, leading to a slight increase in the maximum merger mass in the isotropic model without significantly altering the merger rate.

5. CONCLUSION

We carried out a set of AGN simulations to model AGN-assisted black hole mergers. In particular, we aimed to determine the maximum black hole mass expected to be observed from AGNs as a function of binary and AGN parameters (see Table 1). We examined, through multiple simulations, the dependence of the maximum mass on each of our model parameters, while keeping all other parameters at its fiducial value to be able to explore the 24-dimensional pa-

parameters space (see Fig. 12 and 10). Our conclusions are the following.

1. We found the most substantive change in the maximum mass is related to the lifetime of the AGN disk, t_{AGN} . The maximum attainable mass appears to exponentially grow with t_{AGN} .
2. We find that a black hole mass of $\gtrsim 200 M_{\odot}$ is only attainable for AGN lifetimes $\gtrsim 40$ Myr, independently of the other parameters. Therefore, the possible future detection of such a high-mass black hole in a merger, and the identification of the host AGN through electromagnetic followup, would give a unique measurement of the minimum lifetime of an AGN disk.
3. Several other parameters affect the maximum mass more significantly, in particular the SMBH mass (M_{SMBH}), the angular momentum transport rate (m_{AM}), the disk viscosity parameter (α_{SS}), conversion efficiency (ϵ), and the AGN disk size ($r_{\text{disk,in}}$, $r_{\text{disk,out}}$).
4. The remaining model parameters have limited / marginal effect on the expected maximum black hole

mass. This substantially simplifies the task of constraining the remaining model parameters with observations.

5. The production of a $\sim 100 M_{\odot}$ black hole, like the one in GW190521, requires one of the above parameters to deviate from our fiducial model.
6. We similarly find the dependence of the AGN-assisted merger rate as a function of each of our model parameters (see Figs. 11 and 10), which can also be used to constrain the AGN scenario once it becomes sufficiently clear what subset of the observed black hole mergers are of AGN origin.

The authors are thankful for Yang Yang and Yue Yu for valuable discussions and assistance with the programming process. H.T. was supported by the National Key R&D Program of China (Grant No. 2021YFC2203002). Z.H. is grateful for support from NASA under Grants 80NSSC22K0822 and 80NSSC24K0440. I.B. acknowledges support from the National Science Foundation under Grant No. PHY-2309024.

REFERENCES

- Aasi, J., Abbott, B. P., Abbott, R., et al. 2015, *Classical and Quantum Gravity*, 32, 074001, doi: [10.1088/0264-9381/32/7/074001](https://doi.org/10.1088/0264-9381/32/7/074001)
- Abbott, R., Abbott, T. D., Abraham, S., et al. 2021, *Physical Review X*, 11, 021053, doi: [10.1103/PhysRevX.11.021053](https://doi.org/10.1103/PhysRevX.11.021053)
- . 2020, *PhRvL*, 125, 101102, doi: [10.1103/PhysRevLett.125.101102](https://doi.org/10.1103/PhysRevLett.125.101102)
- Acernese, F., et al. 2015, *Class. Quant. Grav.*, 32, 024001, doi: [10.1088/0264-9381/32/2/024001](https://doi.org/10.1088/0264-9381/32/2/024001)
- Akutsu, T., et al. 2019, *Nature Astron.*, 3, 35, doi: [10.1038/s41550-018-0658-y](https://doi.org/10.1038/s41550-018-0658-y)
- Baker, J. G., Boggs, W. D., Centrella, J., et al. 2007, *The Astrophysical Journal*, 668, 1140
- Bartos, I., Kocsis, B., Haiman, Z., & Márka, S. 2017, *ApJ*, 835, 165, doi: [10.3847/1538-4357/835/2/165](https://doi.org/10.3847/1538-4357/835/2/165)
- Baruteau, C., Cuadra, J., & Lin, D. 2010, *The Astrophysical Journal*, 726, 28
- Baruteau, C., Meru, F., & Paardekooper, S.-J. 2011, *Monthly Notices of the Royal Astronomical Society*, 416, 1971
- Belczynski, K. 2020, *ApJL*, 905, L15, doi: [10.3847/2041-8213/abcblf](https://doi.org/10.3847/2041-8213/abcblf)
- Bell, K., & Lin, D. 1993, *arXiv preprint astro-ph/9312015*
- Bellovary, J. M., Mac Low, M.-M., McKernan, B., & Ford, K. S. 2016, *The Astrophysical Journal Letters*, 819, L17
- Benacquista, M. J., & Downing, J. M. B. 2013, *Living Reviews in Relativity*, 16, 1, doi: [10.12942/lrr-2013-4](https://doi.org/10.12942/lrr-2013-4)
- Binney, J., & Tremaine, S. 2011, *Galactic dynamics*, Vol. 13 (Princeton university press)
- Burtscher, L., Meisenheimer, K., Tristram, K. R., et al. 2013, *Astronomy & Astrophysics*, 558, A149
- Chabrier, G. 2003, *Publications of the Astronomical Society of the Pacific*, 115, 763
- Chapon, D., Mayer, L., & Teyssier, R. 2013, *Monthly Notices of the Royal Astronomical Society*, 429, 3114
- Davis, B. L., Graham, A. W., & Seigar, M. S. 2017, *Monthly Notices of the Royal Astronomical Society*, 471, 2187
- DeLaurentiis, S., Epstein-Martin, M., & Haiman, Z. 2023, *Monthly Notices of the Royal Astronomical Society*, 523, 1126
- Dors, O., Valerdi, M., Freitas-Lemes, P., et al. 2022, *Monthly Notices of the Royal Astronomical Society*, 514, 5506
- Dutta Roy, P., Mahapatra, P., Samajdar, A., & Arun, K. G. 2025, *arXiv e-prints*, arXiv:2503.11721, doi: [10.48550/arXiv.2503.11721](https://doi.org/10.48550/arXiv.2503.11721)
- Epstein-Martin, M., Tagawa, H., Haiman, Z., & Perna, R. 2025, *Monthly Notices of the Royal Astronomical Society*, staf237
- Fishbach, M., Holz, D. E., & Farr, B. 2017, *ApJL*, 840, L24, doi: [10.3847/2041-8213/aa7045](https://doi.org/10.3847/2041-8213/aa7045)
- Fryer, C. L., Woosley, S. E., & Heger, A. 2001, *ApJ*, 550, 372, doi: [10.1086/319719](https://doi.org/10.1086/319719)

- Gamba, R., Breschi, M., Carullo, G., et al. 2023, *Nature Astronomy*, 7, 11, doi: [10.1038/s41550-022-01813-w](https://doi.org/10.1038/s41550-022-01813-w)
- Gangardt, D., Trani, A. A., Bonnerot, C., & Gerosa, D. 2024, *Monthly Notices of the Royal Astronomical Society*, 530, 3689
- Gayathri, V., Yang, Y., Tagawa, H., Haiman, Z., & Bartos, I. 2021, *The Astrophysical Journal Letters*, 920, L42
- Gayathri, V., Healy, J., Lange, J., et al. 2022, *Nature Astronomy*, 6, 344, doi: [10.1038/s41550-021-01568-w](https://doi.org/10.1038/s41550-021-01568-w)
- Gerosa, D., & Berti, E. 2017, *PhRvD*, 95, 124046, doi: [10.1103/PhysRevD.95.124046](https://doi.org/10.1103/PhysRevD.95.124046)
- Gilbaum, S., & Stone, N. C. 2022, *The Astrophysical Journal*, 928, 191
- Goldreich, P., Lithwick, Y., & Sari, R. 2002, *Nature*, 420, 643
- Goldreich, P., & Tremaine, S. 1979, *Astrophysical Journal*, 233, 857
- Gondán, L., Kocsis, B., Raffai, P., & Frei, Z. 2018, *The Astrophysical Journal*, 860, 5
- Gould, A. 1991, *Astrophysical Journal*, Part 1 (ISSN 0004-637X), vol. 379, Sept. 20, 1991, p. 280-284., 379, 280
- Grishin, E., Gilbaum, S., & Stone, N. C. 2024, *Monthly Notices of the Royal Astronomical Society*, 530, 2114
- Haiman, Z., Kocsis, B., & Menou, K. 2009, *The Astrophysical Journal*, 700, 1952
- Ishibashi, W., & Gröbner, M. 2020, *Astronomy & Astrophysics*, 639, A108
- Jiménez, M. A., & Masset, F. S. 2017, *Monthly Notices of the Royal Astronomical Society*, 471, 4917
- Kanagawa, K. D., Tanaka, H., & Szuszkiewicz, E. 2018, *The Astrophysical Journal*, 861, 140
- Kelley, L. Z., Haiman, Z., Sesana, A., & Hernquist, L. 2019, *Monthly Notices of the Royal Astronomical Society*, 485, 1579
- Kocsis, B. 2022, in *Handbook of Gravitational Wave Astronomy*, ed. C. Bambi, S. Katsanevas, & K. D. Kokkotas, 15, doi: [10.1007/978-981-15-4702-7_15-1](https://doi.org/10.1007/978-981-15-4702-7_15-1)
- Kormendy, J., & Ho, L. C. 2013, *Annual Review of Astronomy and Astrophysics*, 51, 511
- Leigh, N. W., Geller, A. M., McKernan, B., et al. 2018, *Monthly Notices of the Royal Astronomical Society*, 474, 5672
- Li, J., Lai, D., & Rodet, L. 2022, *The Astrophysical Journal*, 934, 154
- Li, R., & Lai, D. 2022, *Monthly Notices of the Royal Astronomical Society*, 517, 1602
- Lyra, W., Paardekooper, S.-J., & Mac Low, M.-M. 2010, *The Astrophysical Journal Letters*, 715, L68
- Mahapatra, P., Chattopadhyay, D., Gupta, A., et al. 2024, *ApJ*, 975, 117, doi: [10.3847/1538-4357/ad781b](https://doi.org/10.3847/1538-4357/ad781b)
- . 2025, *PhRvD*, 111, 023013, doi: [10.1103/PhysRevD.111.023013](https://doi.org/10.1103/PhysRevD.111.023013)
- Mahapatra, P., Gupta, A., Favata, M., Arun, K. G., & Sathyaprakash, B. S. 2021, *ApJL*, 918, L31, doi: [10.3847/2041-8213/ac20db](https://doi.org/10.3847/2041-8213/ac20db)
- Mandel, I., & de Mink, S. E. 2016, *Monthly Notices of the Royal Astronomical Society*, 458, 2634, doi: [10.1093/mnras/stw379](https://doi.org/10.1093/mnras/stw379)
- McConnell, N. J., Ma, C.-P., Gebhardt, K., et al. 2011, *Nature*, 480, 215
- McKernan, B., Ford, K., Lyra, W., & Perets, H. 2012, *Monthly Notices of the Royal Astronomical Society*, 425, 460
- McKernan, B., Ford, K. E. S., Bellovary, J., et al. 2018, *ApJ*, 866, 66, doi: [10.3847/1538-4357/aadae5](https://doi.org/10.3847/1538-4357/aadae5)
- Merritt, D. 1999, arXiv preprint astro-ph/9910546
- Miralda-Escudé, J., & Gould, A. 2000, *The Astrophysical Journal*, 545, 847
- O’Leary, R. M., Kocsis, B., & Loeb, A. 2009, *Monthly Notices of the Royal Astronomical Society*, 395, 2127
- Ostriker, E. C. 1999, *The Astrophysical Journal*, 513, 252
- Paardekooper, S.-J., Baruteau, C., Crida, A., & Kley, W. 2010, *Monthly Notices of the Royal Astronomical Society*, 401, 1950
- Paardekooper, S.-J., & Mellema, G. 2006, *Astronomy & Astrophysics*, 459, L17
- Pan, Z., & Yang, H. 2021, *Physical Review D*, 103, 103018
- Papaloizou, J. C., & Larwood, J. D. 2000, *Monthly Notices of the Royal Astronomical Society*, 315, 823
- Park, K., & Bogdanović, T. 2017, *The Astrophysical Journal*, 838, 103
- Park, K., & Ricotti, M. 2013, *The Astrophysical Journal*, 767, 163
- Peng, P., & Chen, X. 2021, *Monthly Notices of the Royal Astronomical Society*, 505, 1324
- Peters, P. C. 1964, *Physical Review*, 136, B1224
- Postnov, K. A., & Yungelson, L. R. 2014, *Living Reviews in Relativity*, 17, 1, doi: [10.12942/lrr-2014-3](https://doi.org/10.12942/lrr-2014-3)
- Qian, K., Li, J., & Lai, D. 2024, *The Astrophysical Journal*, 962, 143
- Rodriguez, C. L., Chatterjee, S., & Rasio, F. A. 2016, *PhRvD*, 93, 084029, doi: [10.1103/PhysRevD.93.084029](https://doi.org/10.1103/PhysRevD.93.084029)
- Romero-Shaw, I., Lasky, P. D., Thrane, E., & Calderón Bustillo, J. 2020, *ApJL*, 903, L5, doi: [10.3847/2041-8213/abbe26](https://doi.org/10.3847/2041-8213/abbe26)
- Rowan, C., Boekholt, T., Kocsis, B., & Haiman, Z. 2023, *Monthly Notices of the Royal Astronomical Society*, 524, 2770
- Rowan, C., Whitehead, H., Boekholt, T., Kocsis, B., & Haiman, Z. 2024a, *Monthly Notices of the Royal Astronomical Society*, 527, 10448
- Rowan, C., Whitehead, H., & Kocsis, B. 2024b, arXiv preprint arXiv:2412.12086
- Salpeter, E. E. 1955, *Astrophysical Journal*, vol. 121, p. 161, 121, 161
- Samsing, J., Bartos, I., D’Orazio, D. J., et al. 2022, *Nature*, 603, 237, doi: [10.1038/s41586-021-04333-1](https://doi.org/10.1038/s41586-021-04333-1)

- Santini, A., Gerosa, D., Cotesta, R., & Berti, E. 2023, *Physical Review D*, 108, 083033
- Sirko, E., & Goodman, J. 2003, *Monthly Notices of the Royal Astronomical Society*, 341, 501
- Tagawa, H., Haiman, Z., Bartos, I., & Kocsis, B. 2020, *ApJ*, 899, 26, doi: [10.3847/1538-4357/aba2cc](https://doi.org/10.3847/1538-4357/aba2cc)
- Tagawa, H., Haiman, Z., Bartos, I., & Kocsis, B. 2020a, *The Astrophysical Journal*, 899, 26
- Tagawa, H., Haiman, Z., & Kocsis, B. 2020b, *The Astrophysical Journal*, 898, 25
- Tagawa, H., Kocsis, B., Haiman, Z., et al. 2021, *The Astrophysical Journal*, 908, 194
- Tanaka, H., Takeuchi, T., & Ward, W. R. 2002, *The Astrophysical Journal*, 565, 1257
- Thompson, T. A., Quataert, E., & Murray, N. 2005, *The Astrophysical Journal*, 630, 167
- Tichy, W., & Marronetti, P. 2008, *Physical Review D—Particles, Fields, Gravitation, and Cosmology*, 78, 081501
- Torres, G., Andersen, J., & Giménez, A. 2010, *The Astronomy and Astrophysics Review*, 18, 67
- Vaccaro, M. P., Mapelli, M., Périgois, C., et al. 2024, *Astronomy & Astrophysics*, 685, A51
- van den Heuvel, E. P. J., Portegies Zwart, S. F., & de Mink, S. E. 2017, *Monthly Notices of the Royal Astronomical Society*, 471, 4256, doi: [10.1093/mnras/stx1430](https://doi.org/10.1093/mnras/stx1430)
- Ward, W. R. 1997, *Icarus*, 126, 261
- Yang, Y., Bartos, I., Haiman, Z., et al. 2019, *The Astrophysical Journal*, 876, 122
- Yang, Y., Gayathri, V., Bartos, I., et al. 2020, *ApJL*, 901, L34, doi: [10.3847/2041-8213/abb940](https://doi.org/10.3847/2041-8213/abb940)
- Yang, Y., Bartos, I., Gayathri, V., et al. 2019, *PhRvL*, 123, 181101, doi: [10.1103/PhysRevLett.123.181101](https://doi.org/10.1103/PhysRevLett.123.181101)